

Eliminating Delocalization Error to Improve Heterogeneous Catalysis Predictions with Molecular DFT+U

Akash Bajaj^{1,2} and Heather J. Kulik^{1,*}

¹*Department of Chemical Engineering, Massachusetts Institute of Technology, Cambridge, MA*

02139

²*Department of Materials Science and Engineering, Massachusetts Institute of Technology,*

Cambridge, MA 02139

ABSTRACT: Approximate semi-local density functional theory (DFT) is known to underestimate surface formation energies yet paradoxically overbind adsorbates on catalytic transition-metal oxide surfaces due to delocalization error. The low-cost DFT+U approach only improves surface formation energies for early transition-metal oxides or adsorption energies for late transition-metal oxides. In this work, we demonstrate that this inefficacy arises due to the conventional usage of metal-centered atomic orbitals as projectors within DFT+U. We analyze electron density rearrangement during surface formation and O atom adsorption on rutile transition-metal oxides to highlight that a standard DFT+U correction fails to tune properties when the corresponding density rearrangement is highly delocalized across both metal and oxygen sites. To improve both surface properties simultaneously while retaining the simplicity of a single-site DFT+U correction, we systematically construct multi-atom-centered molecular-orbital-like projectors for DFT+U. We demonstrate this molecular DFT+U approach for tuning adsorption energies and surface formation energies of minimal two-dimensional models of representative early (i.e., TiO₂) and late (i.e., PtO₂) transition-metal oxides. Molecular DFT+U simultaneously corrects adsorption energies and surface formation energies of multi-layer models of rutile TiO₂(110) and PtO₂(110) to resolve the paradoxical description of surface stability and surface reactivity of semi-local DFT.

1. Introduction

Density functional theory (DFT) using approximate exchange-correlation (xc) functionals remains the primary quantum mechanical method of choice in computational modeling of heterogeneous catalysis¹⁻⁶. However, semi-local xc approximations exhibit both one⁷⁻¹⁰ and many-electron⁹⁻¹² self-interaction error (SIE), commonly referred to as delocalization error¹³⁻¹⁵ (DE). DE leads to an erroneous prediction of dissociation energies^{9,16-18}, reaction barrier heights¹⁹⁻²², adsorption energies^{20,23-25} or adsorption site preferences²⁶⁻³⁰ and surface energies³¹⁻³³ within semi-local DFT, properties that are crucial for an accurate modeling of heterogeneous catalysis. This has given rise to the development and application of both improved semi-local-DFT-based xc functionals targeted towards surface modeling³⁴⁻⁴⁰ and approaches that attempt to reduce DE itself⁴¹⁻⁴³.

One widely adopted approach for reducing DE is the use of hybrid xc functionals incorporating some amount of one-SIE-free exact Hartree–Fock (HF) exchange⁴³⁻⁴⁶. Hybrid functionals can improve the prediction of dissociation or adsorption⁴⁷⁻⁵² energies, of reaction barrier heights⁵³⁻⁵⁵ and of adsorption site preferences⁵⁶⁻⁵⁸ (e.g., CO on Pt(111)). However, hybrid functionals simultaneously incur a larger computational cost relative to semi-local DFT⁵⁹⁻⁶¹ within plane-wave implementations, making them cost-prohibitive for high-throughput studies for the design and discovery of novel heterogeneous catalysts.

A commonly used alternative for reducing DE at the low cost of semi-local DFT is the DFT+U correction scheme⁶²⁻⁶⁶. In its simplified form^{64,65}, the DFT+U energetic correction:

$$E^{\text{DFT+U}} = E^{\text{DFT}} + \frac{1}{2} \sum_{I,nl} \sum_{\sigma} U_{nl}^I [\text{Tr}\{\mathbf{n}_{nl}^{I,\sigma} (\mathbf{1} - \mathbf{n}_{nl}^{I,\sigma})\}], \quad (1)$$

is determined by the U parameter and the occupation matrices, \mathbf{n} , of the subshell nl and spin σ at atomic site I :

$$\{\mathbf{n}_{nl}^{I,\sigma}\}_{mm'} = \sum_{k,v} \langle \psi_{k,v} | \phi_m^I \rangle \langle \phi_m^I | \psi_{k,v} \rangle, \quad (2)$$

obtained using the projections of extended states, $\psi_{k,v}$, on atomic orbitals (AOs), ϕ^I . In typical applications of DFT+U, these projection AOs, ϕ^I , are the d AOs of transition-metal sites that are particularly prone to DE due to their well-localized d electrons⁶⁶. Hence, the DFT+U scheme has been routinely employed for an improved description of the structural, electronic and catalytic properties of transition-metal-containing surfaces⁶⁷⁻⁷⁴.

In heterogeneous catalysis modeling, a severe challenge for semi-local DFT that necessitates the use of such DE reduction approaches is a simultaneously accurate description of the stability and reactivity of surfaces⁷⁵⁻⁷⁸. Specifically, semi-local DFT describes surfaces containing transition metals to be too stable by underestimating their surface formation energy^{31,75,76,79}:

$$E_\sigma = \frac{E_{\text{slab}} - NE_{\text{bulk}}}{2A}, \quad (3)$$

where E_{slab} and E_{bulk} denote the energies of the surface and the bulk models respectively, A is the surface area and N is the ratio of the number of atoms in the surface model to those in the bulk model. At the same time, semi-local DFT paradoxically binds adsorbates on these surfaces too strongly.^{23,24,75,76}

Although both approaches reduce the DE, hybrid functionals and DFT+U are known to correct semi-local DFT errors in transition-metal-containing systems in a divergent fashion^{76,80-82}. In previous work⁷⁶, this divergence was demonstrated in the modeling of surface stability and surface reactivity of transition-metal dioxides that are promising catalysts for the oxygen evolution reaction during electrochemical water splitting⁸³⁻⁹⁰. It was observed that tuning the HF exchange fraction within hybrid DFT improved both surface energy, E_σ , and surface reactivity

(i.e., ΔE_O) in these systems with respect to correlated wavefunction theory references. ΔE_O is computed using the O atom adsorption energy:

$$\Delta E_O = E(O^*) - E(*) - \{E(H_2O) - E(H_2)\}, \quad (4)$$

where $E(*)$ denotes the energy of the pristine surface and $E(O^*)$ denotes the energy of the surface with the O atom adsorbate. In contrast, tuning the U parameter within DFT+U only improved either the description of surface stability or surface reactivity of transition-metal oxides depending on the early (e.g., Ti and V) versus late (e.g., Ir and Pt) nature of the metal.

The inability to tune both surface properties with standard DFT+U may not be a failure of the functional form of the $+U$ correction, which should never worsen the DE⁹¹. Nevertheless, the standard approach has been observed to be inefficient in reducing the DE in some transition-metal-containing systems⁹¹⁻⁹⁵. Pathological examples for DFT+U have been demonstrated in molecular transition-metal complexes where there is strong metal–ligand hybridization (e.g., $Mn(CO)_6$), near-degenerate outer-valence electronic structure due to weak-field ligands (e.g., $Fe(H_2O)_6$), or for metal centers with a closed-shell electronic configuration^{91,92}. Although the standard DFT+U approach is frequently employed for an improved prediction of electronic properties of transition-metal oxides, it has been noted to have limited effect on materials with a closed-shell electronic structure^{93,95,96}. Characteristics associated with delocalization error for transition-metal oxides also gives rise to limitations while using DFT+U to model their structural^{33,97}, electronic^{98,99} and catalytic properties^{100,101}.

Small effects on DE and related properties with application of moderate values of U in DFT+U may be resolved by the application of U on the outer-valence metal s AOs^{93,100,102} and on the AOs of the metal-connecting atoms^{33,96,97,103,104}. However, the choice of appropriate AOs on which the U needs to be applied requires an inspection of the electronic structure of the system

of interest and further requires the determination and tuning of multiple U parameters. We recently proposed an alternative approach for transition-metal complexes where a single U parameter applied using systematically selected frontier molecular orbitals (MOs) as the projection orbitals, ϕ^I , reduces DE much more efficiently, especially for the pathological cases⁹². Similar approaches have also been found to improve adsorption site preferences on transition-metal surfaces^{28,105} and electronic properties of transition-metal oxides and their surfaces¹⁰⁶⁻¹⁰⁸.

Though the low-cost approach of molecular DFT+ U has found success in modeling electronic properties of transition metal systems, its potential as a systematic low-cost approach for simultaneously improving the paradoxical description of surface stability and reactivity of transition-metal oxides has yet to be determined. In this work, we demonstrate the use of the low-cost molecular DFT+ U approach for simultaneously improving E_σ and ΔE_O of rutile transition-metal oxides with efficiency comparable to that of higher computational cost hybrid xc functionals. We establish a systematic protocol for constructing chemically meaningful multi-atom-centered projectors that capture significant metal–oxygen hybridization changes during surface formation and O atom adsorption. Using this procedure, we highlight how the molecular DFT+ U approach improves the semi-local DFT description of both surface reactivity and surface stability across early and late transition-metal oxides while bypassing the larger computational cost incurred by hybrid functionals. The rest of this article is outlined as follows. In Section 2, we provide the computational details of the calculations employed in this work. In Section 3, we analyze density redistribution during surface formation and O atom adsorption for early and late rutile transition-metal oxide surfaces and demonstrate the use of a molecular DFT+ U approach

on representative two-dimensional and multi-layer rutile transition-metal oxide surfaces. Finally, in Section 4, we provide our conclusions.

2. Computational Details.

Structure Preparation. All initial structures were built using the Atomic Simulation Environment (ASE)¹⁰⁹ toolkit v3.16.2. Bulk structures of the rutile-type tetragonal transition-metal dioxides, MO_2 ($\text{M} = \text{Ti}, \text{V}, \text{Ru}, \text{Rh}, \text{Ir}, \text{Pt}$), were generated using the experimental lattice parameters obtained from the Inorganic Crystal Structure Database (ICSD)¹¹⁰ (Supporting Information Table S1). Structures for all (110) surface models were generated using the corresponding DFT-relaxed bulk lattice parameters at each level of theory and consisted of 15 Å of vacuum. Three-dimensional (3D) slabs were modeled using 2×1 unit cells that consisted of four trilayers (i.e., O–M–O repeats). The two-dimensional (2D) layers were modeled with the smallest unit cell to capture all unique metal sites: a 1×1 unit cell for surface energies in PtO_2 and a 2×1 unit cell for adsorption energies in TiO_2 . Initial bond lengths between the metal adsorption site and the adsorbate O atom were always set to expected distances corresponding to chemisorption (i.e., < 2.0 Å, Supporting Information Table S2 and Figures S1–S2).

DFT Calculations. DFT and DFT+U calculations^{62–64,66} with standard atomic projectors on the d states were carried out with the plane-wave periodic boundary condition code Quantum-ESPRESSO¹¹¹ v5.1, using the PBE¹¹² semi-local generalized gradient approximation (GGA) to the exchange-correlation (xc) functional. The Hubbard U was employed in increments of 1 eV (e.g., from 0 to 10 eV), as indicated throughout the text. Ultrasoft pseudopotentials^{113,114} (USPPs) were employed throughout, which were obtained from the Quantum-ESPRESSO website¹¹⁵ (Supporting Information Table S3). Plane-wave cutoffs for all calculations were 35 Ry for the wavefunction and 350 Ry for the charge density⁷⁶. The default convergence threshold of 1×10^{-6}

Ry for the self-consistent field (SCF) energy error was used. To aid SCF convergence, an electronic temperature of 0.005 Hartree was applied and the mixing factor was reduced to 0.4 from its default value of 0.7.

Geometry optimizations were carried out using the BFGS quasi-Newton algorithm¹¹⁶⁻¹²⁰ with default convergence thresholds of 1×10^{-3} Ry/bohr for the maximum residual force and 1×10^{-4} Ry for the change in energy. Lattice parameters and atomic positions of all bulk MO_2 crystals were optimized using $12 \times 12 \times 12$ Monkhorst–Pack k -point grids (Supporting Information Table S1). Atomic positions were optimized for the 3D slab models using a smaller $4 \times 4 \times 1$ Monkhorst–Pack k -point grid. Only the outermost trilayers were optimized for the pristine 3D slab models and only the two topmost trilayers and the adsorbate atom were optimized for the decorated 3D slab models. All atomic positions were optimized for the 2D slab models using a $4 \times 9 \times 1$ Monkhorst–Pack k -point grid for the PtO_2 layer and $4 \times 4 \times 1$ Monkhorst–Pack k -point grid for the TiO_2 layer.

Wannier Functions. Plane-wave eigenstates $|\psi_{k,v}\rangle$ were converted into real-space Wannier functions¹²¹ using the pmw.x utility available with the Quantum-ESPRESSO package for use as MO projectors in DFT+U (Supporting Information Text S1). All eigenstates were generated at the PBE level of theory (Supporting Information Table S4). Relevant eigenstates were selected (see Sec. 3b and Sec. 3c) by specifying a contiguous range for the band index, v , using the “first_band” and “last_band” keywords (Supporting Information Text S1). The MOP DFT+U properties were evaluated from single-point energies using the PBE optimized geometry with U values applied to the MOPs ranging from 0 eV (i.e., PBE) to up to 5 eV in 1 eV increments. This step was necessary because forces are not available for DFT+U with the Wannier function-based MO basis, but comparisons for AO-based DFT+U were optimized

structures could be used indicated a limited effect of geometry changes (Supporting Information Table S5).

Density and Partial Charge Analysis. Electron density cube files were obtained using the `pp.x` postprocessing utility of Quantum-ESPRESSO. The grid resolutions were manually specified to ensure equivalent grid point spacing for computing density differences (Supporting Information Table S6). Extraction of the density in the (110) plane was carried out using an in-house BASH script, and the density difference was computed using an in-house MATLAB script. All structures and three-dimensional densities were visualized using VESTA¹²² v3.3.9. Löwdin partial charges¹²³ were computed using the `projwfc.x` utility of Quantum-ESPRESSO.

3. Results and Discussion.

3a. Density Delocalization Effects on Surface and Adsorption Energies.

Surface formation energies (E_σ , see eq. (3)) of rutile dioxides have previously been observed to be too low with semi-local DFT, as has the tendency of hybrids and DFT+U to correct this error to differing degrees.⁷⁶ Specifically, the sensitivity of E_σ for the $\text{MO}_2(110)$ surface to the U value in DFT+U, $S_U(E_\sigma)$, was similar in magnitude to that from Hartree–Fock (HF) exchange tuning in hybrids, $S_{HF}(E_\sigma)$ only for early transition-metal dioxides (e.g., Ti and V, Supporting Information Table S7). In contrast, later transition metals (TMs) (e.g., Rh and Pt) had very low $S_U(E_\sigma)$ values for the (110) plane in comparison to equivalent $S_{HF}(E_\sigma)$ values (Supporting Information Table S7). One reason why $S_U(E_\sigma)$ could be so low is that there might be significant changes in metal–oxygen hybridization during surface formation that are not detected with a Hubbard U projector applied only to the d states of the metal atoms of later TMs. To understand if that is the reason for d -filling dependence of $S_U(E_\sigma)$, we analyzed the electron

density variation at both the metal and oxygen atom sites for early and later TM surface formation.

We first computed the electron density difference in the $\text{MO}_2(110)$ plane by subtracting a 2D density slice of the 3D grid between the bulk rutile oxide and the pristine slab (Figure 1 and Supporting Information Figures S3–S8). The density redistribution that occurs in this plane is qualitatively different for earlier (e.g., Ti, V) and later (e.g., Rh, Pt) TMs even though they all have the same qualitative MO_2 geometric structures. For the earlier TMs, the density change upon surface cleavage is fairly localized on the surface metal site (Figure 1 and Supporting Information Figures S3–S4). This observation, combined with their relatively high $S_U(E_\sigma)$ values⁷⁶, suggests that a standard DFT+U approach (i.e., with metal-centered atomic orbital projectors) adequately detects an increase in delocalization during surface formation. For the later TMs, electron density redistribution is balanced between surface metal and oxygen sites (Figure 1 and Supporting Information Figures S5–S8). Although one might expect estimates of density redistribution to be sensitive to the choice of plane¹²⁴, modest variations (ca. $\pm 0.08 \text{ \AA}$) in choice of the plane position for analysis do not alter our observations (Supporting Information Figures S3–S8). Taken together with a low $S_U(E_\sigma)$ value for the representative PtO_2 case, this observation indicates that the rehybridization involving both the metal and oxygen that occurs for later TMs cannot be adequately detected within a standard DFT+U approach.

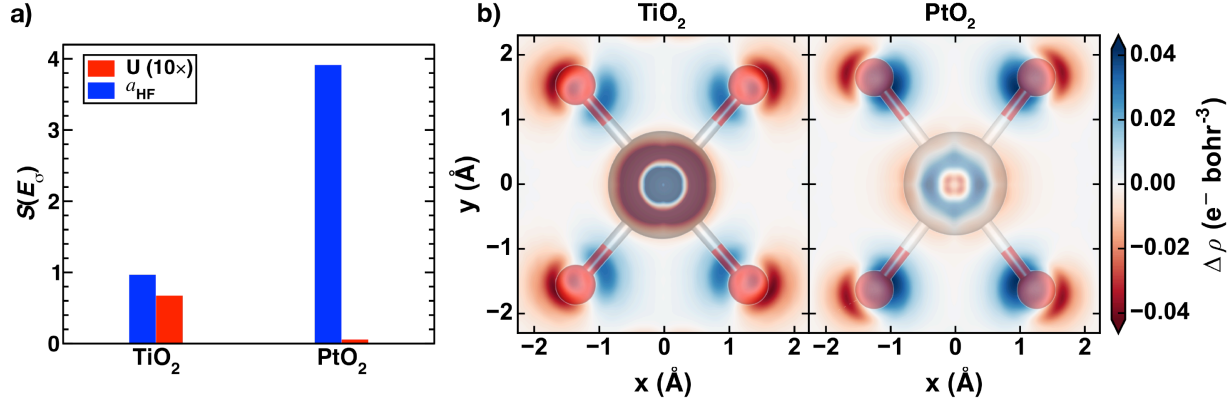


Figure 1. (a) Linearized sensitivity of the surface formation energy, $S(E_\sigma)$, for the (110) planes of rutile TiO_2 and PtO_2 . Sensitivities were computed with respect to the U value (red bars) in units of $\text{eV}/(110)$ u.a. per eV of U (and multiplied by 10) or were obtained from Ref. ⁷⁶ (in $\text{eV}/(110)$ u.a. per HFX) where it was computed with respect to a change in the Hartree–Fock (HF) exchange fraction, a_{HF} , from 0 to 1 i.e., 1 HFX unit (blue bars). (b) Density difference, $\Delta\rho$, (in e^-/bohr^3) between the pristine slab and the bulk rutile models of TiO_2 (left) and PtO_2 (right) computed on the (110) plane. Red indicates density loss and blue indicates density addition evaluated after the surface has been cleaved. Translucent models of the metal atom (gray sphere) and the four coordinating oxygen atoms (red spheres) are overlaid.

We quantified the relative contribution of the in-plane density redistribution at the metal and the oxygen sites by integrating the absolute density difference, $|\Delta\rho|$, on the (110) plane within a 2D circular region centered on the two sites (Supporting Information Figure S9). For earlier TM oxides, the metal-local integrated planar density contribution was more than twice as large as compared to that for late TM oxides. This early TM metal-local contribution was so large that it was comparable to those from all the four coordinating oxygen atoms combined (i.e., roughly 50% of the total density difference) (Supporting Information Table S8). For the later TM oxides, the metal-local contribution to the planar density redistribution was comparatively less (i.e., 25–28%). This d -filling-specific trend of the integrated density difference is independent of the definition of the radius of the oxygen atom (Supporting Information Figure S9). Hence, significant oxygen-centered contributions to density changes for later TM oxides suggest that a multi-atom-centered projector basis will be required to obtain higher DFT+ U surface formation energy sensitivities.

In comparison to surface formation energies, DFT+U and hybrid tuning on oxygen-atom adsorption energies (ΔE_O , see eq. (4)) of rutile dioxides were shown to exhibit opposite trends.⁷⁶ Specifically, the sensitivity of ΔE_O with DFT+U (i.e., $S_U(\Delta E_O)$) was higher for later TMs (e.g., Rh and Pt) and negligible for early TMs (e.g., Ti and V), while Hartree–Fock (HF) exchange tuning (i.e., $S_{HF}(\Delta E_O)$) is large for all rutile dioxides (Supporting Information Table S9). Because we correlated changes in surface metal–oxygen hybridization to $S_U(E_\sigma)$ values, we expect that the nature of changes in surface metal–oxygen (M–O) and metal–adsorbate-oxygen (M–O*) hybridization should rationalize relative $S_U(\Delta E_O)$ values.

To identify trends with d filling, we computed the electron density difference over the entire $\text{MO}_2(110)$ slab model after adsorption (i.e., of a $\frac{1}{2}$ monolayer of O atoms) and analyzed the three-dimensional density difference, $\Delta\rho$, near the adsorption site as a proxy for changes in M–O hybridization (Figure 2 and Supporting Information Figure S10). The density redistribution during adsorption exhibits qualitative differences between early and late TMs (Figure 2 and Supporting Information Figure S10). For the late TM oxide PtO_2 , the density redistribution within the (110) plane upon adsorption is mostly localized on the metal and secondarily on the adsorbing oxygen (Figure 2). This large $\Delta\rho$ local to the metal corresponds to changes in the electron occupations of the metal d atomic orbitals⁷⁶ upon adsorption, meaning that a standard atomic basis for DFT+U can be expected to produce substantial $S_U(\Delta E_O)$ values for the later TMs (Figure 2 and Supporting Information Table S9). In contrast, for the early TM oxide TiO_2 , the density redistribution is highly delocalized on the (110) plane and away from the surface metal site. This delocalization of the density redistribution decreases from early to late TMs (V to Ru or Rh in Supporting Information Figure S10). Such a significant change in the M–O

hybridization away from the metal site corresponds to the much lower $S_U(\Delta E_O)$ values for early TMs with a U applied only on the metal-local d states.

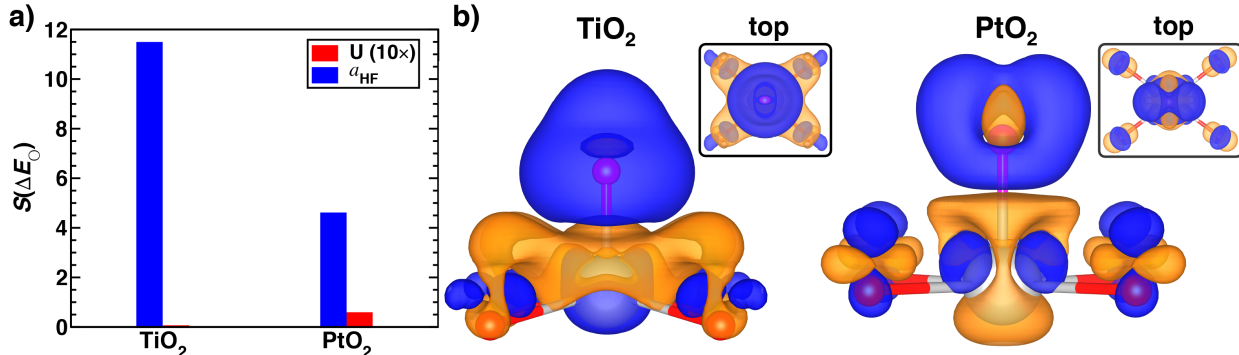


Figure 2. (a) Linearized sensitivity of the adsorption energy, $S(\Delta E_O)$, for the adsorption of 0.5 monolayer of oxygen atoms (O^*) on the (110) plane of rutile TiO_2 and PtO_2 . Sensitivities were computed with respect to the U value (red bars) in units of eV/eV of U (and multiplied by 10) or were obtained from Ref. ⁷⁶ (in eV/HFX) where it was computed with respect to a change in the Hartree–Fock (HF) exchange fraction, a_{HF} , from 0 to 1 i.e., 1 HFX unit (blue bars). (b) Isosurfaces for the density difference (isovalue: $0.003 \text{ e}^-/\text{bohr}^3$) between O^* -adsorbed and pristine (110) surfaces of TiO_2 (left) and PtO_2 (right). The metal adsorption site (gray spheres), the four in-plane coordinating O atoms (red spheres), and the O^* adsorbate (pink spheres) are shown in the front view with the top view depicted in the inset. Orange indicates density loss and blue indicates density gain after O^* adsorption.

We further quantified the influence of M– O^* hybridization changes on $S_U(\Delta E_O)$ by computing the maximum absolute $\Delta\rho$ value along the M– O^* bond (Supporting Information Table S10). The maximum absolute $\Delta\rho$ is higher for the early TMs ($> 0.1 \text{ e}^-/\text{\AA}^3$) than for the later TMs ($< 0.1 \text{ e}^-/\text{\AA}^3$). This larger bond-centered density difference in early TM dioxides highlights why a metal-centered DFT+ U approach leads to low values of $S_U(\Delta E_O)$ for early TMs⁷⁶ in comparison to late TMs (Supporting Information Table S9). Taken together with differences in the in-plane rehybridization, we expect that the standard DFT+ U approach with a U applied on metal d states will have a limited effect on ΔE_O . Indeed, S_U values for ΔE_O are consistently below the S_{HF} values for all TMs in comparison to trends in E_σ evaluations, motivating an alternative to atomic d orbitals for the states considered in DFT+ U corrections of adsorption energies (Supporting Information Tables S7 and S9). A possible approach that has

been pursued is to apply a U on both the metal d and oxygen p states^{33,96,125,126}, but this requires the selection of two appropriate U values, which are known to be system- and property-dependent. As an alternative, we next investigate the possibility of a single U value in DFT+ U applied over a multi-atom-centered basis to obtain DFT+ U sensitivities comparable to those obtained from hybrids simultaneously for E_σ and ΔE_O with both early and late TMs.

3b. Studying 2D MO_2 with DFT+ U using Molecular Projectors.

In DFT+ U , the functional form of the correction consists of a U parameter multiplied by the fractionality¹²⁷, $\text{Tr}[\mathbf{n}(\mathbf{1}-\mathbf{n})]$ (see eq. (1)). When DFT+ U is applied in surface science, values of \mathbf{n} are typically computed by projecting the extended states onto the metal-centered d atomic orbitals as projectors (AOPs) (see eq. (2)). To a first-order approximation, the expected value of $S_U(E_\sigma)$ can be predicted by the metal-local fractionality difference⁷⁶ between the surface and the bulk models i.e., $\Delta\text{Tr}[\mathbf{n}(\mathbf{1}-\mathbf{n})]$ computed with PBE (i.e., $U = 0$ eV). Thus, adjusting the projectors to molecular orbital projectors (MOPs) that increase the $\Delta\text{Tr}[\mathbf{n}(\mathbf{1}-\mathbf{n})]$ between surface and bulk can be expected to improve sensitivities by more adequately reflecting the density redistribution that occurs upon surface cleavage. To determine if improvement in sensitivities is feasible with MOPs, we evaluated the effect of projector choice on $S_U(E_\sigma)$ for a 2D model of the representative later TM PtO_2 for which surface formation energies with AOPs in the 3D system were insensitive to DFT+ U .

The choice to analyze a simplified 2D model consisting only of the single top layer in rutile $\text{PtO}_2(110)$ simplifies the evaluation of Wannier functions by requiring consideration of only two unique Pt sites (Figure 3 and Supporting Information Figure S1). To confirm the suitability of this model system, we computed the AOP $\Delta\text{Tr}[\mathbf{n}(\mathbf{1}-\mathbf{n})]$ and confirmed it to be

negligible, with the exfoliation energy (i.e., E_σ for this single layer) changing by < 0.1 eV from $U = 0$ to 5 eV (Figure 3 and Supporting Information Table S11). Because only one Pt site, Pt_s , has Pt–O bonds that break during exfoliation and becomes undercoordinated, we replace the AOPs only at Pt_s with MOPs and leave the AOPs unchanged for the other Pt site, Pt_b (Figure 3 and Supporting Information Figure S1). As a result, the 2D PtO_2 $S_U(E_\sigma)$ should be determined only by the $\Delta\text{Tr}[\mathbf{n}(\mathbf{1}-\mathbf{n})]$ for the new projectors on the Pt_s site. This strategy can be generalized, for example to surface properties of 3D rutile MO_2 systems by retaining AOPs for multiple bulk-like (e.g., subsurface sites in a slab) metal sites (see Sec. 3c).

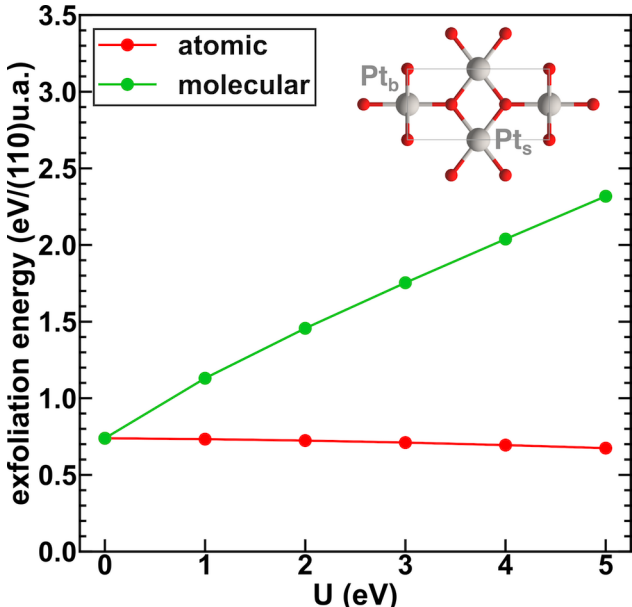


Figure 3. Exfoliation energy of 2D PtO_2 (in $\text{eV}/(110)\text{u.a.}$) computed using different projectors within DFT+U at U values ranging from 0 to 5 eV. Energies were computed using atomic projectors (red) at both Pt sites or replacing only the atomic projectors at the surface undercoordinated Pt site, Pt_s , with the fractionality-selected best molecular projectors constructed using the Wannier localization scheme (green). The top view of the unit cell of 2D PtO_2 is shown in the inset with the Pt_s site annotated.

To construct multi-atom-centered projectors using $\Delta\text{Tr}[\mathbf{n}(\mathbf{1}-\mathbf{n})]$ as the figure of merit, we use the approximate Wannier function (WF) localization scheme implemented in Quantum-ESPRESSO¹¹¹ as in prior work⁹² (Supporting Information Text S1). We must select a set of

contiguous plane-wave states $\{\psi_{\mathbf{k},v}\}$, where \mathbf{k} denotes the k -point and v denotes the band index, and we project them onto the AOPs being replaced (here, the Pt_s 5d AOs). These states are then transformed into five real-space WF projectors, analogous to molecular orbitals as projectors (MOPs) in isolated transition-metal complexes⁹². (Supporting Information Text S1). For both bulk and 2D PtO₂, we select all combinations of five contiguous states from a total of 50 possible states both above and below the Fermi level (Supporting Information Table S4). We thus construct 46 sets of MO-like WF projectors each for bulk and 2D PtO₂ i.e., leading to 2116 possible (i.e., 46×46) pairs. Several criteria exist for selecting a good set of MO projectors to increase the sensitivity of the exfoliation energy to Hubbard U values. Because surface states are more likely to be present near the Fermi level and have partial occupancies, we require a non-zero value of $\text{Tr}[\mathbf{n}(\mathbf{1}-\mathbf{n})]$ (i.e., partial occupancy) of the MO projectors in both bulk and 2D PtO₂ for the Pt_s site (Figure 4). Additionally, we select the MOP pair having the maximum positive $\Delta\text{Tr}[\mathbf{n}(\mathbf{1}-\mathbf{n})]$ between the bulk and the surface because the corresponding states are likely undergoing the most significant change in hybridization during exfoliation (Figure 4). Using these two criteria, we identify a pair of MO projectors for bulk and 2D PtO₂ to maximally increase the $S_U(E_\sigma)$ of 2D PtO₂ (Figure 4). Although we selected a single pair to test our approach, a number of other pairs around the Fermi level would have also satisfied both criteria (Figure 4).

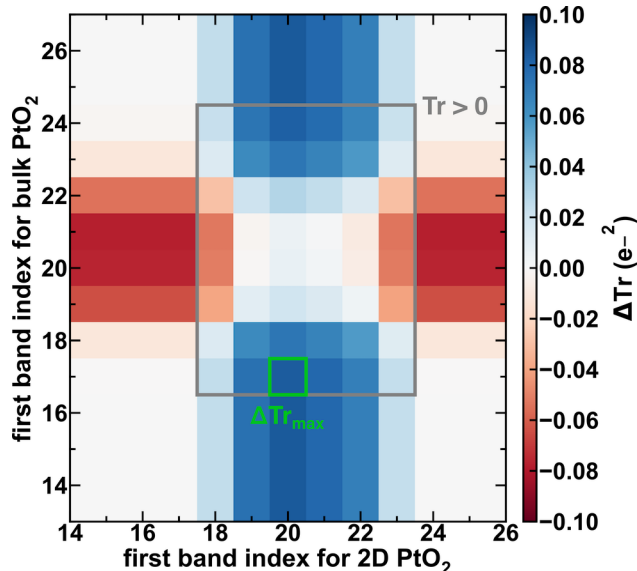


Figure 4. Fractionality difference per orbital, $\Delta\text{Tr}[\mathbf{n}(1-\mathbf{n})]$ (in e^{-2}), between 2D PtO_2 (110) and bulk rutile PtO_2 shown for representative molecular projectors constructed using the Wannier localization scheme for both systems. The index of the first band selected for the Wannier localization for 2D PtO_2 is labeled on the x-axis and the index of the first band selected for the Wannier localization for bulk PtO_2 is labeled on the y-axis. The projector pair having the maximum $\Delta\text{Tr}[\mathbf{n}(1-\mathbf{n})]$ is outlined with a green square, and those having a positive $\text{Tr}[\mathbf{n}(1-\mathbf{n})]$ on Pt_s are outlined with a gray rectangle.

To gain physical intuition for the numerically selected best MOPs, we analyze the real-space (i.e., Γ -point) projected density of states (PDOS) and densities of the selected MOPs for 2D PtO_2 (Figure 5). The selected MO states reside within 1.0–1.5 eV of the Fermi level (Figure 5). As could be expected, the MOs have contributions from both $\text{Pt}(5d)$ and $\text{O}(2p)$ AOs, but do not have a majority contribution from $\text{Pt}(5d)$, unlike the standard AOPs (Supporting Information Table S12). Another distinct feature of all the MOs is the prominent contribution ($>15\%$) from the $\text{O}(2p_z)$ AOs where the z -axis is perpendicular to the (110) plane (Figure 5). We expect $\text{O}(2p_z)$ AO contributions to be important because their out-of-plane electron density is likely to get redistributed during exfoliation due to changes in the local bonding environment. Indeed, no other set of five contiguous states were found to have as large $\text{O}(2p_z)$ AO contributions as the ones selected by our figure of merit (Supporting Information Table S12).

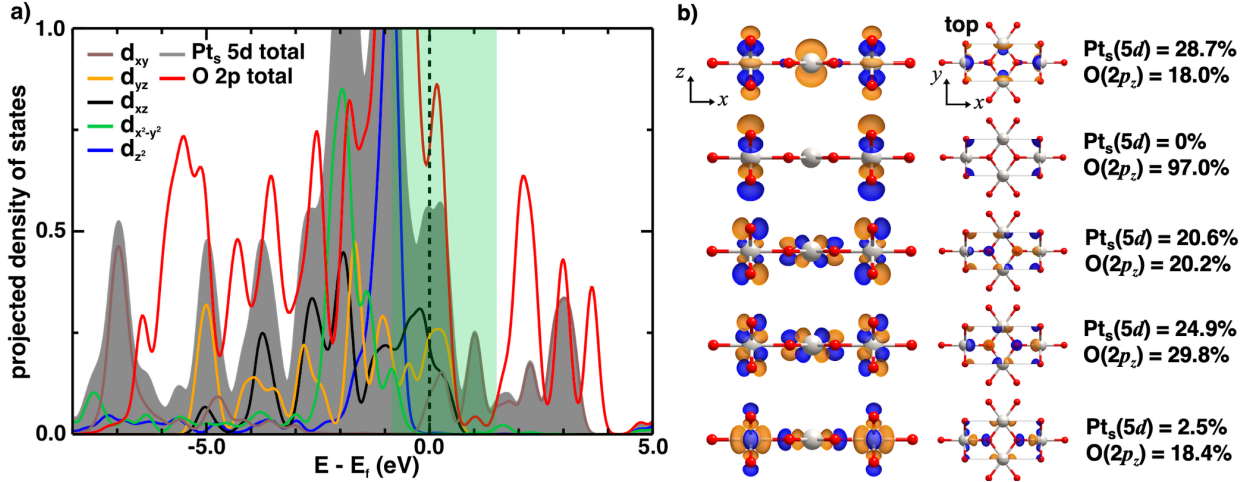


Figure 5. (a) Γ -point projected density of states (PDOS) of all Pt_s(5d) atomic orbitals (gray shaded region) and all nearest-neighbor O(2p) atomic orbitals (red solid line) in 2D PtO₂(110). PDOS for the $5d_{xy}$, $5d_{yz}$, $5d_{xz}$, $5d_{x^2-y^2}$ and $5d_{z^2}$ atomic orbitals are also indicated using brown, orange, black, green, and blue solid lines respectively. The vertical black dashed line indicates the Fermi level (E_f) while the green transparent region represents the states selected for constructing the molecular projectors within the Wannier localization scheme. (b) Γ -point density isosurfaces (isovalue = 0.005 e⁻/bohr³) of the five molecular projectors for 2D PtO₂. Blue indicates positive wavefunction phase and orange indicates negative wavefunction phase. States are ordered in increasing energy from top to bottom. Views along both the y-axis and the z-axis are shown with Pt_s(5d) and O(2p_z) contributions annotated. Pt and O atoms are shown as gray and red spheres respectively.

To validate the effect of MOPs on DFT+U energy corrections, we computed the exfoliation energy of 2D PtO₂(110) (i.e., E_σ) with increasing U values (Figure 3 and Supporting Information Table S11). Compared to the negligible change in E_σ observed with AOPs, E_σ obtained using MO projectors increases by more than 1.5 eV over a 5 eV increase in U , which corresponds to a twenty-fold increase in $S_U(E_\sigma)$. Clearly, the construction of MOPs using Wannier localization and fractionality-based metrics provides us with physically justified multi-atom-centered projectors having higher $S_U(E_\sigma)$ than possible with metal-centered AOPs. Moreover, the use of such a projector choice facilitates the tuning of E_σ using a single U parameter.

We next investigated how the use of MOPs influences early TM cases (e.g., TiO₂) where standard AOPs led to low sensitivities to applied U for oxygen adsorption, $S_U(\Delta E_O)$, and test our

approach on a 2D monolayer. We again focus on the 2D model due to the smaller number of sites and bands over which we need to select and evaluate Wannier-based MOPs (Supporting Information Figure S2). We estimate the expected $S_U(\Delta E_O)$ with AOPs for this system from the fractionality difference, $\Delta\text{Tr}[\mathbf{n}(1-\mathbf{n})]$ at $U = 0$ eV, between the surface with adsorbed O and the pristine surface⁷⁶. As expected, the $\Delta\text{Tr}[\mathbf{n}(1-\mathbf{n})]$ for O atom adsorption on 2D TiO₂(110) is negligible with DFT+U using AOPs (i.e., < 0.01 eV/eV of U , Figure 6 and Supporting Information Table S13).

We replace the AOPs with MOPs for the adsorption site, Ti_s, and treat the other two Ti sites in this 2D TiO₂ model (i.e., Ti_b and Ti_u) with standard AOPs (Figure 6 and Supporting Information Figure S2). Similar to the case of PtO₂, we select all combinations of five contiguous states from a total of 75 possible bands both below and above the Fermi energy for the pristine or the O*-decorated 2D TiO₂ (Supporting Information Text S1 and Table S4). This combination leads to 5041 possible sets (i.e., 71×71) of pairs of MOPs because the band index need not be identical for the two (i.e., pristine and adsorbed) 2D TiO₂ models. We use the same two criteria we applied for $S_U(E_\sigma)$, i.e., $\text{Tr}[\mathbf{n}(1-\mathbf{n})] > 0$ for the MOPs and a maximum value of $\Delta\text{Tr}[\mathbf{n}(1-\mathbf{n})]$, to identify a single best pair of MO projectors (Supporting Information Figure S11).

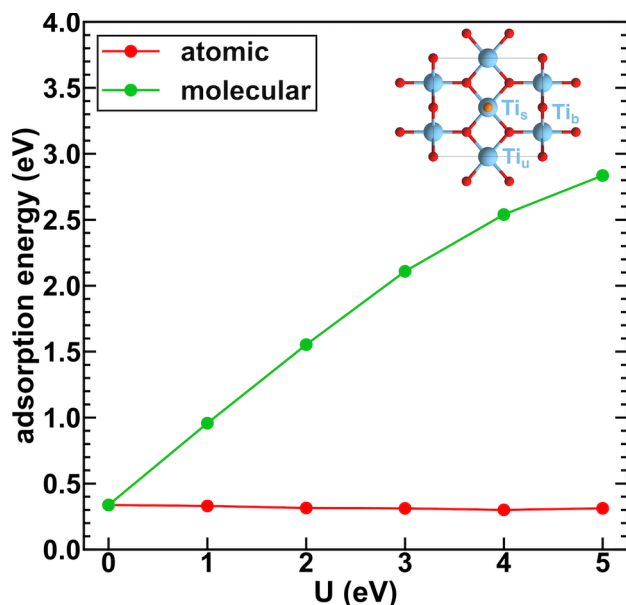


Figure 6. Adsorption energy (in eV) for a $\frac{1}{2}$ monolayer of O on 2D $\text{TiO}_2(110)$ computed using different projectors within DFT+U at U values ranging from 0 to 5 eV. Energies were computed using atomic projectors (red) at all three Ti sites or replacing the atomic projectors only at the site of adsorption, Ti_s , with the fractionality-selected best molecular projectors constructed using the Wannier localization scheme (green). The top view of the unit cell of the O^* adsorbate containing 2D TiO_2 is shown in the inset. Ti atoms are shown in blue, O atoms are shown in red, the adsorbate O^* atom is shown in orange, and the Ti_s site is annotated.

The fractionality-selected MO states lie within 1.5 eV of the Fermi level (i.e., both above and below) for the O^* -decorated 2D TiO_2 whereas the corresponding MO states for the pristine TiO_2 layer all lie within 1.5 eV below its Fermi level (Figure 7 and Supporting Information Figure S12). The $\text{O}(2p)$ AO contributions from surface oxygen atoms are $> 40\%$ for the MOPs in both models and significantly outweigh the $\text{Ti}_s(3d)$ contributions ($< 10\%$) in all MOPs (Figure 7 and Supporting Information Tables S14–S15). In particular, for the adsorbed model, the TiO_2 MOPs have a prominent ($> 35\%$) contribution from the $\text{O}^*(2p)$ states, which follows our expectations of what would be required to obtain positive $S_U(\Delta E_O)$ values. These MOPs corresponds to weak π^* interactions, as indicated by a mixture of $\text{Ti}_s(3d_{xz})$ and $\text{Ti}_s(3d_{yz})$ AOs with O $\text{O}^*(2p)$ states. The MOPs corresponding to stronger Ti– O^* σ overlap lie well below the Fermi level and are fully occupied (i.e., $\text{Tr} = 0$), leading them not to be selected by fractionality

analysis (Supporting Information Table S15). Furthermore, no other set of five contiguous states were found to have as large $O^*(2p)$ AO contributions (Supporting Information Table S15).

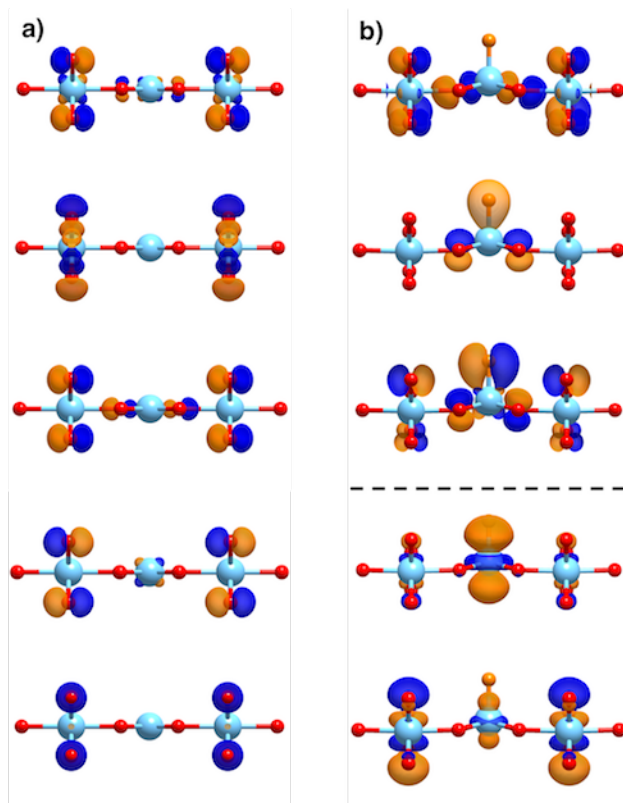


Figure 7. Γ -point density isosurfaces (isovalue = $0.002 \text{ e}^-/\text{bohr}^3$) of the five fractionality-selected best molecular projectors for (a) pristine 2D TiO_2 and (b) O^* -decorated 2D TiO_2 shown in the side view. Blue indicates positive wavefunction phase and orange indicates negative wavefunction phase. States are ordered in increasing energy from top to bottom, where energies of all states for pristine 2D TiO_2 were lower than its Fermi level and only the states above the black horizontal dashed line for O^* -decorated 2D TiO_2 had energies lower than its Fermi level. Ti, O and adsorbate O^* atoms are shown as blue, red and orange spheres respectively.

Finally, we validated the suitability of these MOPs by computing the ΔE_O of 2D $\text{TiO}_2(110)$ with increasing U values (Figure 6 and Supporting Information Table S13). For the fractionality-selected MOPs, the ΔE_O increases by 2.5 eV over a 5 eV increase in U , resulting in an $S_U(\Delta E_O)$ increase of a factor of more than 80 relative to the AOPs. While these selected MOPs can be expected to yield the largest sensitivities, they have asymmetric contributions of $\text{Ti}_s(3d_{xz})$ and $\text{Ti}_s(3d_{yz})$ AOs and thus break the degeneracy of these states. We therefore also considered an

alternative, contiguous set of five MOPs by adjusting the selection until there was an equal contribution from both $\text{Ti}_s(3d_{xz})$ and $\text{Ti}_s(3d_{yz})$ AOs. While this set does not produce the maximum sensitivity (i.e., as judged by our $\Delta\text{Tr}[\mathbf{n}(1-\mathbf{n})]$ figure of merit), it still significantly exceeds that obtained with AOPs (Supporting Information Tables S13–S14). This alternate MOP selection results in an $S_U(\Delta E_O)$ higher by a factor of more than 70 relative to the AOPs. Thus, one could directly focus on constructing physical, symmetric MOPs based on intuition to achieve the same result of relatively high sensitivities, but it would be harder to automate. Overall, MOPs constructed using Wannier localization and fractionality-based metrics are able to yield higher $S_U(\Delta E_O)$ in comparison to the use of AOPs.

3c. Simultaneous Tuning of Surface Formation and Adsorption Energies for MO_2 Slabs.

We then asked whether our MOP approach could simultaneously tune $S_U(E_\sigma)$ and $S_U(\Delta E_O)$ in 3D (i.e., slab) multi-layer models of rutile MO_2 . For the later TMs, we return to the prototypical case of PtO_2 , where tuning U in the standard DFT+U approach destabilizes O atom adsorption (i.e., high $S_U(\Delta E_O)$) but has no effect on the surface formation energy (i.e., low $S_U(E_\sigma)$)⁷⁶. We treat all distinct Pt sites uniquely and replace the projectors only at the Pt sites involved in Pt–O bond breaking in surface formation or those involved in Pt–O* adsorption (i.e., Pt_u and Pt_s sites) (Supporting Information Figure S1). For the single Pt_s site in bulk rutile PtO_2 , we replace the five Pt_s d AO projectors with five MOPs, leading to 46 possible combinations of five contiguous states from the total 50 available both above and below the Fermi level (Figure 8 and Supporting Information Table S4). For pristine and O*-decorated $\text{PtO}_2(110)$ surface models that contain four such Pt sites (i.e., Pt_s or Pt_u), we now need to replace a total of 20 Pt $5d$ AOs with 20 MOPs (Supporting Information Figure S1). Thus, for each of the two surface models, we

select all possible combinations of 20 contiguous states from the total 250 available to construct 231 sets of MOPs (Figure 8 and Supporting Information Table S4). After constructing the MOP sets, we determine the best possible pairs of sets that maximize the effect of Hubbard U on the properties of interest using the same criteria as before. Specifically, we compute $\text{Tr}[\mathbf{n}(\mathbf{1}-\mathbf{n})]$ for each MOP set, require it to be positive, and compute $\Delta\text{Tr}[\mathbf{n}(\mathbf{1}-\mathbf{n})]$ for each MOP pair relevant to both the E_σ and ΔE_O properties (Figure 8). The $S_U(E_\sigma)$ and $S_U(\Delta E_O)$ are influenced by the difference (i.e., $\Delta\text{Tr}[\mathbf{n}(\mathbf{1}-\mathbf{n})]$) between the pristine and bulk models and between the decorated and pristine models respectively. Hence, if the dangling bonds or adsorbate-involved MOs are the most different between these two reference states, the $\Delta\text{Tr}[\mathbf{n}(\mathbf{1}-\mathbf{n})]$, and thus the sensitivities, should be maximized for the MOPs (Figure 8). We observe that a large number of pairs satisfy these two criteria (Figure 8). Generally, higher-energy orbitals are preferred for the pristine slab in the case of the adsorption energy than for surface formation, but a range of 10–20 starting band numbers is suitable for both, whereas a narrower range of band indices is suitable for the smaller bulk system (Figure 8).

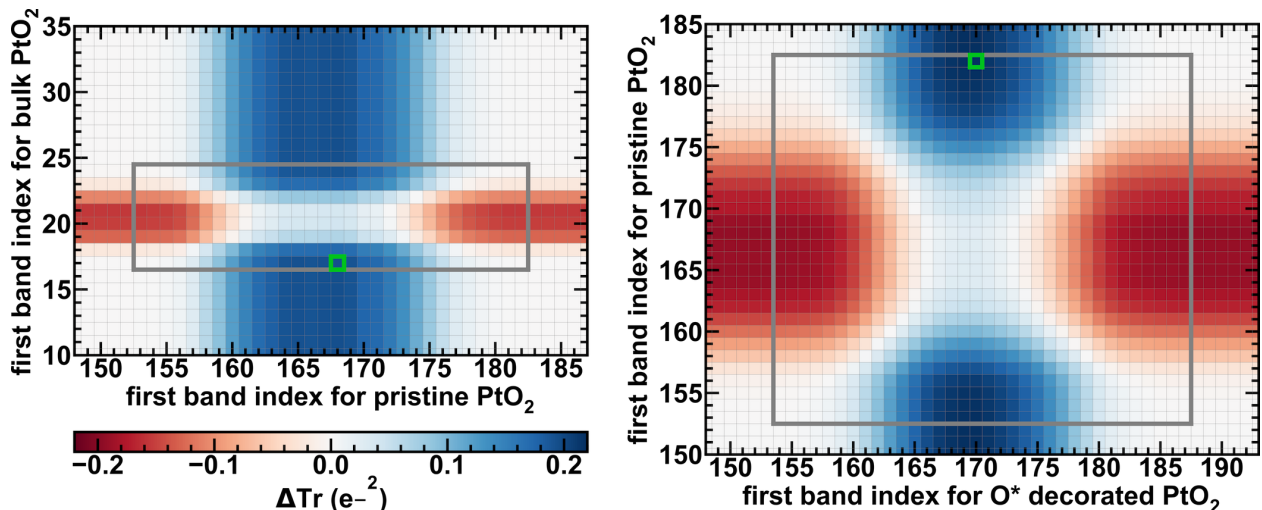


Figure 8. Fractionality difference per orbital, $\Delta\text{Tr}[\mathbf{n}(\mathbf{1}-\mathbf{n})]$ (in e^{-2}), between representative molecular projectors constructed using the Wannier localization scheme of the pristine $\text{PtO}_2(110)$ surface and bulk rutile PtO_2 (left) and of O^* -decorated and pristine $\text{PtO}_2(110)$ surfaces (right). Values on the x and y axes show the index of the first band selected for Wannier localization in

the indicated system. The projector pair having the maximum $\Delta\text{Tr}[\mathbf{n}(1-\mathbf{n})]$ is outlined with a green square and those having a positive Tr are outlined with a gray rectangle.

As could be expected from our criteria, the best MOPs are within 3 eV of the Fermi level for all models (Supporting Information Figures S13–S15). For bulk PtO_2 , the selected MOPs predominantly consist of $\text{O}(2p)$ states and are thus distinct from the metal-centered AOPs in standard DFT+U (Supporting Information Figure S13). For both the pristine and O^* -adsorbed $\text{PtO}_2(110)$ surface models, most of the selected MOPs also have $\text{O}(2p)$ contributions that are higher than or comparable to the $\text{Pt}(5d)$ contributions (Supporting Information Tables S16–S17). Thus, projectors that discriminate the properties of the bulk from either the pristine or decorated slab must directly address differences in oxygen orbital occupations. For example, the $\text{Pt}(5d)$ contributions to the pristine $\text{PtO}_2(110)$ slab MOPs selected for $S_U(E_\sigma)$ predominantly consist of out-of-plane $\text{Pt}(5d_{z^2})$ AOs (Supporting Information Figure S14). For O^* -decorated $\text{PtO}_2(110)$ MOPs relevant to $S_U(\Delta E_O)$, a large contribution (ca. 40–55%) comes from the $\text{O}^*(2p)$ AO (Supporting Information Figure S15 and Table S17). Thus, while our MOPs are empirically selected to maximize fractionality differences, our criteria naturally led to selection of MOPs that reflect the chemical bonding changes between the states being compared.

Finally, we use the fractionality-selected best MOPs to evaluate E_σ and ΔE_O for PtO_2 and the corresponding linearized DFT+U sensitivities (Figure 9). We observe that the use of the best selected MOPs achieves our goal of tuning both properties substantially more than the use of AOPs. In fact, the MOP DFT+U sensitivities are one to two orders of magnitude higher than the AOP DFT+U sensitivities, suggesting the possibility of using lower U values for these best selected MOPs, which can have the advantage of improving calculation convergence in practice^{66,128}. Most importantly, MOPs simultaneously tune E_σ and ΔE_O for the late transition-metal oxide PtO_2 . The fractionality-selected best MOPs for the pristine $\text{PtO}_2(110)$ model are

different for tuning E_σ and ΔE_O (Figure 8 and Supporting Information Table S16). To reduce any ambiguity this introduces, we selected a compromise set of contiguous MOPs for the pristine $\text{PtO}_2(110)$ slab that were near the Fermi level (i.e., $\text{Tr}[\mathbf{n}(\mathbf{1}-\mathbf{n})]$ is positive) and contained AO contributions (i.e., both $\text{O}(2p)$ and out of plane $\text{Pt}(5d_{z^2})$) that gave the best $\Delta\text{Tr}[\mathbf{n}(\mathbf{1}-\mathbf{n})]$ for both calculations simultaneously (Supporting Information Table S16 and Figure S16). This selection of MOPs for the pristine $\text{PtO}_2(110)$ slab still leads to DFT+U sensitivities that are an order of magnitude higher than the AOP sensitivities for both quantities (Supporting Information Figure S16). Thus, the MOP DFT+U sensitivities are now able to reproduce trends that were previously only achievable with a single parameter when carried out with HF exchange tuning (Figure 9 and Supporting Information Tables S7 and S9).

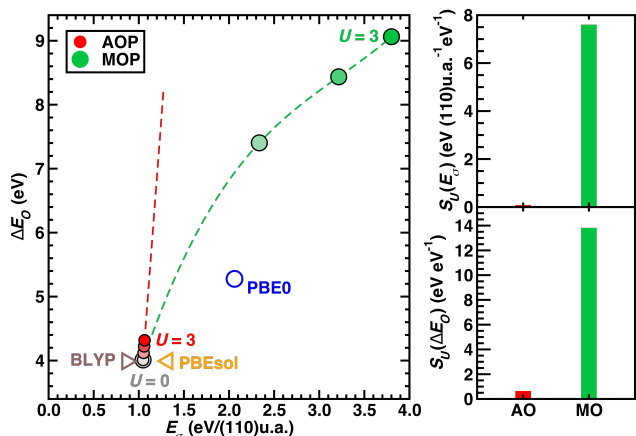


Figure 9. (left) ΔE_O (in eV) versus E_σ (in eV/(110)u.a.) for PtO_2 (110) computed using the Pt $5d$ AOPs (shaded red circles) and the fractionality-selected best MOPs (shaded green circles) at integer values of U from 0 to 3 eV with a dashed line indicating the trend between these points. Values from BLYP^{129,130} (brown triangle), PBEsol³⁷ (orange triangle), and PBE0^{131,132} (blue circle) were obtained from Ref. ⁷⁶ using a localized basis set and shifted to align our PBE plane-wave basis set value and the PBE localized basis set value from Ref. ⁷⁶. (right) Linearized sensitivities of E_σ (top, in eV/(110) unit area per eV of U) and of ΔE_O (bottom, in eV per eV of U) computed with AOPs (red bars) and MOPs (green bars).

We used the fractionality-based selection protocol for constructing MOPs for TiO_2 , a representative early transition-metal oxide where DFT+U with AOPs only tuned E_σ (Supporting Information Tables S18–S19). This selection method again yields frontier MOPs from states that

lie near the Fermi level (Supporting Information Tables S18–S19). At odds with the standard metal-centered Ti(3*d*) AOPs, the selected MOPs have substantial O(2*p*) contributions (i.e., more than Ti(3*d*)) contributions for both pristine and decorated TiO₂(110), especially O(2*p_z*) contributions to the MOPs selected for tuning E_σ (Supporting Information Tables S18–S19). Similarly, states having majority O*(2*p*) AO character are selected for tuning ΔE_O of TiO₂(110) (Supporting Information Tables S19).

We used these fractionality-selected MOPs to evaluate E_σ and ΔE_O along with their corresponding sensitivities for TiO₂ (Figure 10). The MOP-based DFT+U sensitivities are high for both quantities, with magnitudes comparable to HF exchange sensitivities that simultaneously improve both E_σ and ΔE_O with respect to expectations and reference values (Figure 10 and Supporting Information Tables S7 and S9). Similarly, a contiguous “compromise” set of pristine TiO₂(110) slab frontier MOPs with majority O(2*p*) AO contributions that maximized the overall $\Delta\text{Tr}[\mathbf{n}(\mathbf{1}-\mathbf{n})]$ for both adsorption and surface energy calculations enabled simultaneous tuning of both quantities and higher sensitivities than the AOP-based DFT+U approach (Supporting Information Figure S17). Thus, this MOP approach enables an automated strategy to tune both surface formation energies and adsorption energies from their semi-local DFT values regardless of the nature of the transition metal with performance comparable to hybrids but within a low-cost DFT+U framework.

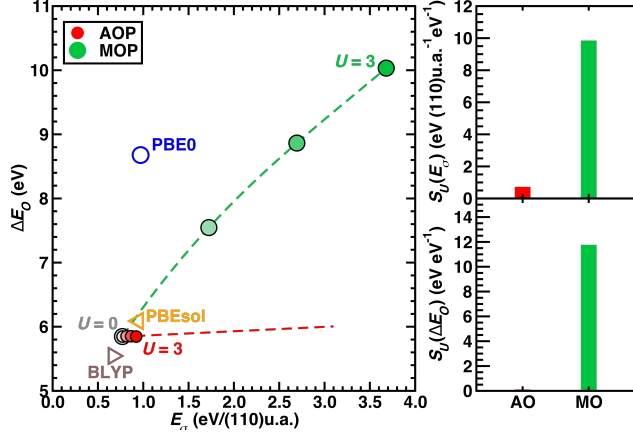


Figure 10. (left) ΔE_O (in eV) versus E_σ (in eV/(110)u.a.) for TiO_2 (110) computed using the Ti 3d AOPs (shaded red circles) and the fractionality-selected best MOPs (shaded green circles) at integer values of U from 0 to 3 eV with a dashed line indicating the trend between these points. Values from BLYP^{129,130} (brown triangle), PBEsol³⁷ (orange triangle), and PBE0^{131,132} (blue circle) were obtained from Ref. ⁷⁶ using a localized basis set and shifted to align our PBE plane-wave basis set value and the PBE localized basis set value from Ref. ⁷⁶. (right) Linearized sensitivities of E_σ (top, in eV/(110) unit area per eV of U) and of ΔE_O (bottom, in eV per eV of U) computed with AOPs (red bars) and MOPs (green bars).

4. Conclusions.

We investigated the previously identified limitations of the standard DFT+U approach in simultaneously tuning adsorption energies and surface energies of transition-metal (TM) oxide surfaces. We demonstrated the benefit of using molecular-orbital-like extended projectors (MOPs) for overcoming these limitations within a DFT+U framework. We justified these improvements by analyzing electron density differences between the materials compared in energetic calculations (i.e., the bulk, pristine slabs, and decorated slabs), confirming that standard DFT+U with AOPs tuned the relevant property only when the corresponding density redistribution (e.g., from bulk to pristine slab) was predominantly metal centered. This helped us to rationalize the high sensitivity for surface formation but low sensitivity for adsorption energies in early TMs (e.g., Ti, V) that exhibited metal-local density redistribution during surface formation but a relatively delocalized density redistribution during O atom adsorption, and vice versa for late TMs (e.g., Pt, Ru).

Given the benefit of moving to multi-atom-centered projectors, we developed a systematic protocol for constructing the MOPs to use in DFT+U. Using guiding principles to select sets of frontier orbitals, we were able to identify chemically relevant extended states for MOPs that maximally tuned E_σ of the representative late TM PtO₂ and ΔE_O of the representative early TM TiO₂. In both cases, the selected MOPs were distinct from the standard metal-centered d AOPs, with the MOPs instead having majority O($2p$) AO character. Moreover, our protocol highlighted distinctive characteristics of MOPs required for tuning E_σ or ΔE_O , with surface O($2p_z$) contributions key for E_σ and adsorbate O*($2p$) contributions important for ΔE_O tuning.

We extended our MOP construction scheme for tuning both properties in 3D slabs of TiO₂(110) and PtO₂(110). The resulting MOP-based DFT+U sensitivities were one to two orders of magnitude higher than those previously obtained using standard DFT+U. This increased sensitivity reduced the value of U needed to tune surface properties, which is beneficial because high values of U in standard DFT+U are known to introduce challenges for convergence of the self-consistent field and over-elongate bonds. The other benefits of this approach are that it maintains a low-cost relative to hybrids and minimizes the number of adjustable parameters in comparison to multi-site DFT+U. We expect this approach to be broadly applicable to a range of surfaces where hybridization is present that normally cannot be addressed with DFT+U. To reduce empiricism, the DFT+U MOPs could be selected to reproduce hybrid functional results or experimental benchmarks, where available.

ASSOCIATED CONTENT

Supporting Information Available. This material is available free of charge via the Internet at <http://pubs.acs.org>.

Lattice parameters of all bulk rutile transition-metal oxides with +U correction; PBE-level metal-adsorbate bond lengths; overview of approach for constructing and using molecular-orbital-like projectors (i.e., Wannier functions) with DFT+U; influence of geometry optimization on energies at low U values; AOP-based DFT+U or HF surface formation energy and adsorption energy sensitivities for all transition-metal oxides; density difference between bulk rutile and pristine surface for all transition-metal oxides near the (110) plane; illustration of the integration scheme used for quantifying density difference between bulk rutile and pristine (110) surface, shown for a representative transition-metal oxide and integral values for all transition-metal oxides; qualitative density difference between pristine and O*-decorated (110) surfaces for oxides of V, Ru, Rh and Ir; quantitative density difference between pristine and O*-decorated (110) surfaces along the M-O* bond for all transition-metal oxides; diagram of unique metal site indexing in all models of TiO₂ and PtO₂; total number of eigenstates generated at the PBE-level for all models of TiO₂ and PtO₂ that were used for constructing and testing all possible MOPs; AO contributions of all eigenstates for 2D TiO₂ and PtO₂; fractionality-based selection of MOPs for tuning 2D TiO₂ adsorption energy and PDOS analysis of its fractionality-selected best MOPs; fractionalities and DFT+U sensitivities using AOPs and best MOPs for tuning 2D PtO₂ exfoliation energy and 2D TiO₂ adsorption energy; PDOS analysis and AO contributions of best MOPs for 3D PtO₂ models; AO contributions of best MOPs for 3D TiO₂ models; 3D TiO₂ and PtO₂ surface energetics using consistent MOPs for the pristine model; grid resolutions used for generating all electron density cube files and pseudopotentials used for all calculations (PDF)

Structures of all materials studied in this work (ZIP)

AUTHOR INFORMATION

Corresponding Author

*email: hjkulik@mit.edu phone: 617-253-4584

Notes

The authors declare no competing financial interest.

ACKNOWLEDGMENT

This material is based upon work supported by the Department of Energy, National Nuclear Security Administration under Award Number DE-NA0003965. This work made use of Department of Defense HPCMP computing resources. H.J.K. holds a Career Award at the Scientific Interface from the Burroughs Wellcome Fund, an AAAS Marion Milligan Mason

Award, and an Alfred P. Sloan award in Chemistry, which supported this work. The authors thank Chenru Duan, Aditya Nandy, Adam H. Steeves, and Vyshnavi Vennelakanti for providing a critical reading of the manuscript.

References

- (1) Norskov, J. K.; Scheffler, M.; Toulhoat, H. Density Functional Theory in Surface Science and Heterogeneous Catalysis. *MRS Bull.* **2006**, *31*, 669.
- (2) Bennett, J. W.; Jones, D. T.; Hamers, R. J.; Mason, S. E. First-Principles and Thermodynamics Study of Compositionally Tuned Complex Metal Oxides: Cation Release from the (001) Surface of Mn-Rich Lithium Nickel Manganese Cobalt Oxide. *Inorg. Chem.* **2018**, *57*, 13300.
- (3) Xu, S. Z.; Carter, E. A. Theoretical Insights into Heterogeneous (Photo)Electrochemical CO₂ Reduction. *Chem. Rev.* **2019**, *119*, 6631.
- (4) Rousseau, R.; Glezakou, V. A.; Selloni, A. Theoretical Insights into the Surface Physics and Chemistry of Redox-Active Oxides. *Nat. Rev. Mater.* **2020**, *5*, 460.
- (5) Li, X. Y.; Chiong, R.; Hu, Z. Y.; Page, A. J. Low-Cost Pt Alloys for Heterogeneous Catalysis Predicted by Density Functional Theory and Active Learning. *J. Phys. Chem. Lett.* **2021**, *12*, 7305.
- (6) Chen, B. W. J.; Xu, L.; Mavrikakis, M. Computational Methods in Heterogeneous Catalysis. *Chem. Rev.* **2021**, *121*, 1007.
- (7) Grafenstein, J.; Kraka, E.; Cremer, D. The Impact of the Self-Interaction Error on the Density Functional Theory Description of Dissociating Radical Cations: Ionic and Covalent Dissociation Limits. *J. Chem. Phys.* **2004**, *120*, 524.
- (8) Lundberg, M.; Siegbahn, P. E. M. Quantifying the Effects of the Self-Interaction Error in DFT: When Do the Delocalized States Appear? *J. Chem. Phys.* **2005**, *122*, 224103.
- (9) Ruzsinszky, A.; Perdew, J. P.; Csonka, G. I.; Vydrov, O. A.; Scuseria, G. E. Density Functionals That Are One- and Two- Are Not Always Many-Electron Self-Interaction-Free, as Shown for H-2(+), He-2(+), LiH+, and Ne-2(+). *J. Chem. Phys.* **2007**, *126*, 104102.
- (10) Schmidt, T.; Kummel, S. One- and Many-Electron Self-Interaction Error in Local and Global Hybrid Functionals. *Phys. Rev. B* **2016**, *93*, 165120.
- (11) Mori-Sanchez, P.; Cohen, A. J.; Yang, W. T. Many-Electron Self-Interaction Error in Approximate Density Functionals. *J. Chem. Phys.* **2006**, *125*, 201102.
- (12) Haunschild, R.; Henderson, T. M.; Jimenez-Hoyos, C. A.; Scuseria, G. E. Many-Electron Self-Interaction and Spin Polarization Errors in Local Hybrid Density Functionals. *J. Chem. Phys.* **2010**, *133*, 134116.
- (13) Mori-Sanchez, P.; Cohen, A. J.; Yang, W. T. Localization and Delocalization Errors in Density Functional Theory and Implications for Band-Gap Prediction. *Phys. Rev. Lett.* **2008**, *100*, 146401.
- (14) Cohen, A. J.; Mori-Sanchez, P.; Yang, W. T. Insights into Current Limitations of Density Functional Theory. *Science* **2008**, *321*, 792.

- (15) Cohen, A. J.; Mori-Sanchez, P.; Yang, W. T. Challenges for Density Functional Theory. *Chem. Rev.* **2012**, *112*, 289.
- (16) Bally, T.; Sastry, G. N. Incorrect Dissociation Behavior of Radical Ions in Density Functional Calculations. *J. Phys. Chem. A* **1997**, *101*, 7923.
- (17) Dutoi, A. D.; Head-Gordon, M. Self-Interaction Error of Local Density Functionals for Alkali-Halide Dissociation. *Chem. Phys. Lett.* **2006**, *422*, 230.
- (18) Ruzsinszky, A.; Perdew, J. P.; Csonka, G. I.; Vydrov, O. A.; Scuseria, G. E. Spurious Fractional Charge on Dissociated Atoms: Pervasive and Resilient Self-Interaction Error of Common Density Functionals. *J. Chem. Phys.* **2006**, *125*, 194112.
- (19) Johnson, B. G.; Gonzales, C. A.; Gill, P. M. W.; Pople, J. A. A Density-Functional Study of the Simplest Hydrogen Abstraction Reaction - Effect of Self-Interaction Correction. *Chem. Phys. Lett.* **1994**, *221*, 100.
- (20) Janesko, B. G. Density Functional Theory Beyond the Generalized Gradient Approximation for Surface Chemistry. *Top. Curr. Chem.* **2015**, *365*, 25.
- (21) Sharada, S. M.; Bligaard, T.; Luntz, A. C.; Kroes, G. J.; Norskov, J. K. Sb10: A Benchmark Database of Barrier Heights on Transition Metal Surfaces. *J. Phys. Chem. C* **2017**, *121*, 19807.
- (22) Goncalves, T. J.; Plessow, P. N.; Studt, F. On the Accuracy of Density Functional Theory in Zeolite Catalysis. *ChemCatChem* **2019**, *11*, 4368.
- (23) Mason, S. E.; Grinberg, I.; Rappe, A. M. Adsorbate-Adsorbate Interactions and Chemisorption at Different Coverages Studied by Accurate Ab Initio Calculations: Co on Transition Metal Surfaces. *J. Phys. Chem. B* **2006**, *110*, 3816.
- (24) Wellendorff, J.; Silbaugh, T. L.; Garcia-Pintos, D.; Norskov, J. K.; Bligaard, T.; Studt, F.; Campbell, C. T. A Benchmark Database for Adsorption Bond Energies to Transition Metal Surfaces and Comparison to Selected Dft Functionals. *Surf. Sci.* **2015**, *640*, 36.
- (25) Huang, X.; Mason, S. E. Dft-Gga Errors in No Chemisorption Energies on (111) Transition Metal Surfaces. *Surf. Sci.* **2014**, *621*, 23.
- (26) Feibelman, P. J.; Hammer, B.; Norskov, J. K.; Wagner, F.; Scheffler, M.; Stumpf, R.; Watwe, R.; Dumesic, J. The Co/Pt(111) Puzzle. *J. Phys. Chem. B* **2001**, *105*, 4018.
- (27) Hu, Q. M.; Reuter, K.; Scheffler, M. Towards an Exact Treatment of Exchange and Correlation in Materials: Application to the "Co Adsorption Puzzle" and Other Systems. *Phys. Rev. Lett.* **2007**, *98*, 176103.
- (28) Kresse, G.; Gil, A.; Sautet, P. Significance of Single-Electron Energies for the Description of Co on Pt(111). *Phys. Rev. B* **2003**, *68*, 073401.
- (29) Janet, J. P.; Zhao, Q.; Ioannidis, E. I.; Kulik, H. J. Density Functional Theory for Modeling Large Molecular Adsorbate-Surface Interactions: A Mini-Review and Worked Example. *Mol. Simul.* **2017**, *43*, 327.
- (30) Grinberg, I.; Yourdshahyan, Y.; Rappe, A. M. Co on Pt(111) Puzzle: A Possible Solution. *J. Chem. Phys.* **2002**, *117*, 2264.
- (31) De Waele, S.; Lejaeghere, K.; Sluydts, M.; Cottenier, S. Error Estimates for Density-Functional Theory Predictions of Surface Energy and Work Function. *Phys. Rev. B* **2016**, *94*, 235418.
- (32) Cramer, C. J.; Truhlar, D. G. Density Functional Theory for Transition Metals and Transition Metal Chemistry. *Phys. Chem. Chem. Phys.* **2009**, *11*, 10757.
- (33) Huang, X.; Ramadugu, S. K.; Mason, S. E. Surface-Specific Dft Plus U Approach Applied to Alpha-Fe₂O₃(0001). *J. Phys. Chem. C* **2016**, *120*, 4919.

- (34) Sun, J. W.; Marsman, M.; Ruzsinszky, A.; Kresse, G.; Perdew, J. P. Improved Lattice Constants, Surface Energies, and Co Desorption Energies from a Semilocal Density Functional. *Phys. Rev. B* **2011**, *83*, 121410.
- (35) Armiento, R.; Mattsson, A. E. Functional Designed to Include Surface Effects in Self-Consistent Density Functional Theory. *Phys. Rev. B* **2005**, *72*, 085108.
- (36) Hammer, B.; Hansen, L. B.; Norskov, J. K. Improved Adsorption Energetics within Density-Functional Theory Using Revised Perdew-Burke-Ernzerhof Functionals. *Phys. Rev. B* **1999**, *59*, 7413.
- (37) Perdew, J. P.; Ruzsinszky, A.; Csonka, G. I.; Vydrov, O. A.; Scuseria, G. E.; Constantin, L. A.; Zhou, X. L.; Burke, K. Restoring the Density-Gradient Expansion for Exchange in Solids and Surfaces (Vol 100, Art No 136406, 2008). *Phys. Rev. Lett.* **2009**, *102*, 039902.
- (38) Wu, Z. G.; Cohen, R. E. More Accurate Generalized Gradient Approximation for Solids. *Phys. Rev. B* **2006**, *73*, 235116.
- (39) Wellendorff, J.; Lundgaard, K. T.; Mogelhoff, A.; Petzold, V.; Landis, D. D.; Norskov, J. K.; Bligaard, T.; Jacobsen, K. W. Density Functionals for Surface Science: Exchange-Correlation Model Development with Bayesian Error Estimation. *Phys. Rev. B* **2012**, *85*, 235149.
- (40) Mattsson, A. E.; Armiento, R.; Paier, J.; Kresse, G.; Wills, J. M.; Mattsson, T. R. The Am05 Density Functional Applied to Solids. *J. Chem. Phys.* **2008**, *128*, 084714.
- (41) Marsman, M.; Paier, J.; Stroppa, A.; Kresse, G. Hybrid Functionals Applied to Extended Systems. *J. Phys.: Condens. Matter* **2008**, *20*, 064201.
- (42) Heyd, J.; Scuseria, G. E.; Ernzerhof, M. Hybrid Functionals Based on a Screened Coulomb Potential (Vol 118, Pg 8207, 2003). *J. Chem. Phys.* **2006**, *124*, 219906.
- (43) Karolewski, A.; Kronik, L.; Kummel, S. Using Optimally Tuned Range Separated Hybrid Functionals in Ground-State Calculations: Consequences and Caveats. *J. Chem. Phys.* **2013**, *138*, 204115.
- (44) Becke, A. D. Density-Functional Thermochemistry .3. The Role of Exact Exchange. *J. Chem. Phys.* **1993**, *98*, 5648.
- (45) Baer, R.; Livshits, E.; Salzner, U. Tuned Range-Separated Hybrids in Density Functional Theory. *Annu. Rev. Phys. Chem.* **2010**, *61*, 85.
- (46) Janesko, B. G.; Henderson, T. M.; Scuseria, G. E. Screened Hybrid Density Functionals for Solid-State Chemistry and Physics. *Phys. Chem. Chem. Phys.* **2009**, *11*, 443.
- (47) Brugnoli, L.; Pedone, A.; Menziani, M. C.; Adamo, C.; Labat, F. H₂ Dissociation and Water Evolution on Silver-Decorated CeO₂(111): A Hybrid Density Functional Theory Investigation. *J. Phys. Chem. C* **2019**, *123*, 25668.
- (48) Lopez, N.; Illas, F.; Pacchioni, G. Electronic Effects in the Activation of Supported Metal Clusters: Density Functional Theory Study of H₂ Dissociation on Cu/SiO₂. *J. Phys. Chem. B* **1999**, *103*, 8552.
- (49) Janesko, B. G.; Barone, V.; Brothers, E. N. Accurate Surface Chemistry Beyond the Generalized Gradient Approximation: Illustrations for Graphene Adatoms. *Journal of Chemical Theory and Computation* **2013**, *9*, 4853.
- (50) Wellington, J. P. W.; Kerridge, A.; Austin, J.; Kaltsoyannis, N. Electronic Structure of Bulk AnO₂ (an = U, Np, Pu) and Water Adsorption on the (111) and (110) Surfaces of UO₂ and PuO₂ from Hybrid Density Functional Theory within the Periodic Electrostatic Embedded Cluster Method. *J. Nucl. Mater.* **2016**, *482*, 124.

- (51) Lopez, N.; Illas, F. Ab Initio Modeling of the Metal-Support Interface: The Interaction of Ni, Pd, and Pt on MgO(100). *J. Phys. Chem. B* **1998**, *102*, 1430.
- (52) Zhao, Y.; Ng, H. T.; Peverati, R.; Truhlar, D. G. Benchmark Database for Ylidic Bond Dissociation Energies and Its Use for Assessments of Electronic Structure Methods. *Journal of Chemical Theory and Computation* **2012**, *8*, 2824.
- (53) Zheng, J. J.; Zhao, Y.; Truhlar, D. G. The Dbh24/08 Database and Its Use to Assess Electronic Structure Model Chemistries for Chemical Reaction Barrier Heights. *Journal of Chemical Theory and Computation* **2009**, *5*, 808.
- (54) Zhao, Y.; Gonzalez-Garcia, N.; Truhlar, D. G. Benchmark Database of Barrier Heights for Heavy Atom Transfer, Nucleophilic Substitution, Association, and Unimolecular Reactions and Its Use to Test Theoretical Methods. *J. Phys. Chem. A* **2005**, *109*, 2012.
- (55) Karton, A.; Tarnopolsky, A.; Lamere, J. F.; Schatz, G. C.; Martin, J. M. L. Highly Accurate First-Principles Benchmark Data Sets for the Parametrization and Validation of Density Functional and Other Approximate Methods. Derivation of a Robust, Generally Applicable, Double-Hybrid Functional for Thermochemistry and Thermochemical Kinetics. *J. Phys. Chem. A* **2008**, *112*, 12868.
- (56) Doll, K. Co Adsorption on the Pt(111) Surface: A Comparison of a Gradient Corrected Functional and a Hybrid Functional. *Surf. Sci.* **2004**, *573*, 464.
- (57) Stroppa, A. Co Adsorption on Metal Surfaces: A Hybrid Density Functional Study with Plane Wave Basis Set. *J. Phys.: Condens. Matter* **2008**, *20*, 064205.
- (58) Wang, Y.; de Gironcoli, S.; Hush, N. S.; Reimers, J. R. Successful a Priori Modeling of Co Adsorption on Pt(111) Using Periodic Hybrid Density Functional Theory. *J. Am. Chem. Soc.* **2007**, *129*, 10402.
- (59) Chawla, S.; Voth, G. A. Exact Exchange in Ab Initio Molecular Dynamics: An Efficient Plane-Wave Based Algorithm. *J. Chem. Phys.* **1998**, *108*, 4697.
- (60) Chevrier, V. L.; Ong, S. P.; Armiento, R.; Chan, M. K. Y.; Ceder, G. Hybrid Density Functional Calculations of Redox Potentials and Formation Energies of Transition Metal Compounds. *Phys. Rev. B* **2010**, *82*, 075122.
- (61) Mandal, S.; Debnath, J.; Meyer, B.; Nair, N. N. Enhanced Sampling and Free Energy Calculations with Hybrid Functionals and Plane Waves for Chemical Reactions. *J. Chem. Phys.* **2018**, *149*, 144113.
- (62) Anisimov, V. I.; Zaanen, J.; Andersen, O. K. Band Theory and Mott Insulators - Hubbard-U Instead of Stoner-I. *Phys. Rev. B* **1991**, *44*, 943.
- (63) Liechtenstein, A. I.; Anisimov, V. I.; Zaanen, J. Density-Functional Theory and Strong-Interactions - Orbital Ordering in Mott-Hubbard Insulators. *Phys. Rev. B* **1995**, *52*, R5467.
- (64) Dudarev, S. L.; Botton, G. A.; Savrasov, S. Y.; Humphreys, C. J.; Sutton, A. P. Electron-Energy-Loss Spectra and the Structural Stability of Nickel Oxide: An Lsda+U Study. *Phys. Rev. B* **1998**, *57*, 1505.
- (65) Cococcioni, M.; de Gironcoli, S. Linear Response Approach to the Calculation of the Effective Interaction Parameters in the Lda+U Method. *Phys. Rev. B* **2005**, *71*, 035105.
- (66) Kulik, H. J. Perspective: Treating Electron over-Delocalization with the Dft+U Method. *J. Chem. Phys.* **2015**, *142*, 240901.
- (67) Capdevila-Cortada, M.; Garcia-Melchor, M.; Lopez, N. Unraveling the Structure Sensitivity in Methanol Conversion on CeO₂: A Dft + U Study. *J. Catal.* **2015**, *327*, 58.

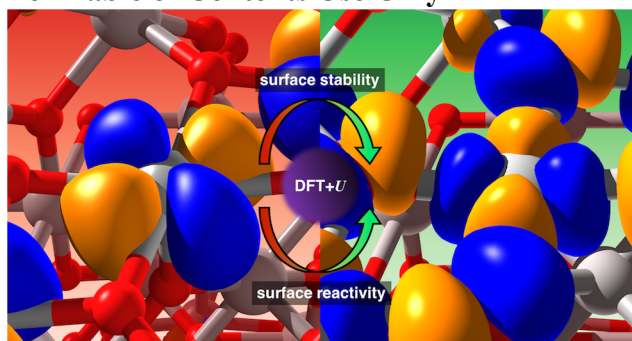
- (68) Capdevila-Cortada, M.; Lodziana, Z.; Lopez, N. Performance of Dft Plus U Approaches in the Study of Catalytic Materials. *ACS Catal.* **2016**, *6*, 8370.
- (69) Lopez, N.; Almora-Barrios, N.; Carchini, G.; Blonski, P.; Bellarosa, L.; Garcia-Muelas, R.; Novell-Leruth, G.; Garcia-Mota, M. State-of-the-Art and Challenges in Theoretical Simulations of Heterogeneous Catalysis at the Microscopic Level. *Catal. Sci. Technol.* **2012**, *2*, 2405.
- (70) Huang, X.; Bennett, J. W.; Hang, M. M. N.; Laudadio, E. D.; Hamers, R. J.; Mason, S. E. Ab Initio Atomistic Thermodynamics Study of the (001) Surface of LiCoO₂ in a Water Environment and Implications for Reactivity under Ambient Conditions. *J. Phys. Chem. C* **2017**, *121*, 5069.
- (71) Kanan, D. K.; Keith, J. A.; Carter, E. A. First-Principles Modeling of Electrochemical Water Oxidation on MnO: ZnO(001). *ChemElectroChem* **2014**, *1*, 407.
- (72) Li, Y. F.; Aschauer, U.; Chen, J.; Selloni, A. Adsorption and Reactions of O₂ on Anatase TiO₂. *Acc. Chem. Res.* **2014**, *47*, 3361.
- (73) Hammes-Schiffer, S.; Galli, G. Integration of Theory and Experiment in the Modelling of Heterogeneous Electrocatalysis. *Nat. Energy* **2021**, *6*, 700.
- (74) Park, K. W.; Kolpak, A. M. Optimal Methodology for Explicit Solvation Prediction of Band Edges of Transition Metal Oxide Photocatalysts. *Commun. Chem.* **2019**, *2*, 79.
- (75) Schimka, L.; Harl, J.; Stroppa, A.; Gruneis, A.; Marsman, M.; Mittendorfer, F.; Kresse, G. Accurate Surface and Adsorption Energies from Many-Body Perturbation Theory. *Nat. Mater.* **2010**, *9*, 741.
- (76) Zhao, Q.; Kulik, H. J. Stable Surfaces That Bind Too Tightly: Can Range Separated Hybrids or Dft+U Improve Paradoxical Descriptions of Surface Chemistry? *J. Phys. Chem. Lett.* **2019**, *10*, 5090.
- (77) Lininger, C. N.; Gauthier, J. A.; Li, W. L.; Rossomme, E.; Welborn, V. V.; Lin, Z.; Head-Gordon, T.; Head-Gordon, M.; Bell, A. T. Challenges for Density Functional Theory: Calculation of Co Adsorption on Electrocatalytically Relevant Metals. *Phys. Chem. Chem. Phys.* **2021**, *23*, 9394.
- (78) Gattinoni, C.; Michaelides, A. Atomistic Details of Oxide Surfaces and Surface Oxidation: The Example of Copper and Its Oxides. *Surf. Sci. Rep.* **2015**, *70*, 424.
- (79) Fishman, M.; Zhuang, H. L. L.; Mathew, K.; Dirschka, W.; Hennig, R. G. Accuracy of Exchange-Correlation Functionals and Effect of Solvation on the Surface Energy of Copper. *Phys. Rev. B* **2013**, *87*, 245402.
- (80) Zhao, Q.; Kulik, H. J. Where Does the Density Localize in the Solid State? Divergent Behavior for Hybrids and Dft+U. *Journal of Chemical Theory and Computation* **2018**, *14*, 670.
- (81) Verma, P.; Truhlar, D. G. Does Dft Plus U Mimic Hybrid Density Functionals? *Theor. Chem. Acc.* **2016**, *135*, 182.
- (82) Brumboiu, I. E.; Haldar, S.; Luder, J.; Eriksson, O.; Herper, H. C.; Brena, B.; Sanyal, B. Influence of Electron Correlation on the Electronic Structure and Magnetism of Transition-Metal Phthalocyanines. *Journal of Chemical Theory and Computation* **2016**, *12*, 1772.
- (83) Hong, W. T.; Risch, M.; Stoerzinger, K. A.; Grimaud, A.; Suntivich, J.; Shao-Horn, Y. Toward the Rational Design of Non-Precious Transition Metal Oxides for Oxygen Electrocatalysis. *Energy Environ. Sci.* **2015**, *8*, 1404.

- (84) Rossmeisl, J.; Qu, Z. W.; Zhu, H.; Kroes, G. J.; Nørskov, J. K. Electrolysis of Water on Oxide Surfaces. *J. Electroanal. Chem.* **2007**, *607*, 83.
- (85) Stoerzinger, K. A.; Qiao, L.; Biegalski, M. D.; Shao-Horn, Y. Orientation-Dependent Oxygen Evolution Activities of Rutile IrO₂ and RuO₂. *J. Phys. Chem. Lett.* **2014**, *5*, 1636.
- (86) Schaub, R.; Thoststrup, P.; Lopez, N.; Laegsgaard, E.; Stensgaard, I.; Nørskov, J. K.; Besenbacher, F. Oxygen Vacancies as Active Sites for Water Dissociation on Rutile TiO₂(110). *Phys. Rev. Lett.* **2001**, *87*, 266104.
- (87) Wu, T. T.; Lopez, N.; Vegge, T.; Hansen, H. A. Facet-Dependent Electrocatalytic Water Splitting Reaction on CeO₂: A Dft + U Study. *J. Catal.* **2020**, *388*, 1.
- (88) Nguyen, H. C.; Garces-Pineda, F. A.; De Fez-Febre, M.; Galan-Mascaros, J. R.; Lopez, N. Non-Redox Doping Boosts Oxygen Evolution Electrocatalysis on Hematite. *Chem. Sci.* **2020**, *11*, 2464.
- (89) Chen, J.; Li, Y. F.; Sit, P.; Selloni, A. Chemical Dynamics of the First Proton-Coupled Electron Transfer of Water Oxidation on TiO₂ Anatase. *J. Am. Chem. Soc.* **2013**, *135*, 18774.
- (90) Rajan, A. G.; Martinez, J. M. P.; Carter, E. A. Why Do We Use the Materials and Operating Conditions We Use for Heterogeneous (Photo)Electrochemical Water Splitting? *ACS Catal.* **2020**, *10*, 11177.
- (91) Zhao, Q.; Ioannidis, E. I.; Kulik, H. J. Global and Local Curvature in Density Functional Theory. *J. Chem. Phys.* **2016**, *145*, 054109.
- (92) Bajaj, A.; Kulik, H. J. Molecular Dft+U: A Transferable, Low-Cost Approach to Eliminate Delocalization Error. *J. Phys. Chem. Lett.* **2021**, *12*, 3633.
- (93) Yu, K.; Carter, E. A. Communication: Comparing Ab Initio Methods of Obtaining Effective U Parameters for Closed-Shell Materials. *J. Chem. Phys.* **2014**, *140*, 121105.
- (94) Li, S. K.; Li, Y.; Baumer, M.; Moskaleva, L. V. Assessment of Pbe+U and Hse06 Methods and Determination of Optimal Parameter U for the Structural and Energetic Properties of Rare Earth Oxides. *J. Chem. Phys.* **2020**, *153*, 164710.
- (95) Brown, J. J.; Page, A. J. Reaction Pathways in the Solid State and the Hubbard U Correction. *J. Chem. Phys.* **2021**, *154*, 124121.
- (96) Brown, J. J.; Page, A. J. The Hubbard-U Correction and Optical Properties of D(0) Metal Oxide Photocatalysts. *J. Chem. Phys.* **2020**, *153*, 224116.
- (97) Linscott, E. B.; Cole, D. J.; Payne, M. C.; O'Regan, D. D. Role of Spin in the Calculation of Hubbard U and Hund's J Parameters from First Principles. *Phys. Rev. B* **2018**, *98*, 235157.
- (98) Mattioli, G.; Alippi, P.; Filippone, F.; Caminiti, R.; Bonapasta, A. A. Deep Versus Shallow Behavior of Intrinsic Defects in Rutile and Anatase TiO₂ Polymorphs. *J. Phys. Chem. C* **2010**, *114*, 21694.
- (99) Hegner, F. S.; Galan-Mascaros, J. R.; Lopez, N. A Database of the Structural and Electronic Properties of Prussian Blue, Prussian White, and Berlin Green Compounds through Density Functional Theory. *Inorg. Chem.* **2016**, *55*, 12851.
- (100) Kulik, H. J.; Cococcioni, M.; Scherlis, D. A.; Marzari, N. Density Functional Theory in Transition-Metal Chemistry: A Self-Consistent Hubbard U Approach. *Phys. Rev. Lett.* **2006**, *97*, 103001.
- (101) Mattioli, G.; Giannozzi, P.; Bonapasta, A. A.; Guidonili, L. Reaction Pathways for Oxygen Evolution Promoted by Cobalt Catalyst. *J. Am. Chem. Soc.* **2013**, *135*, 15353.

- (102) Kulik, H. J.; Marzari, N. Systematic Study of First-Row Transition-Metal Diatomic Molecules: A Self-Consistent Dft Plus U Approach. *J. Chem. Phys.* **2010**, *133*, 114103.
- (103) Orhan, O. K.; O'Regan, D. D. First-Principles Hubbard U and Hund's J Corrected Approximate Density Functional Theory Predicts an Accurate Fundamental Gap in Rutile and Anatase Tio₂. *Phys. Rev. B* **2020**, *101*, 245137.
- (104) Brumboiu, I. E.; Haldar, S.; Luder, J.; Eriksson, E.; Herper, H. C.; Brena, B.; Sanyal, B. Ligand Effects on the Linear Response Hubbard U: The Case of Transition Metal Phthalocyanines. *J. Phys. Chem. A* **2019**, *123*, 3214.
- (105) Gajdos, M.; Hafner, J. Co Adsorption on Cu(111) and Cu(001) Surfaces: Improving Site Preference in Dft Calculations. *Surf. Sci.* **2005**, *590*, 117.
- (106) Fabris, S.; Vicario, G.; Balducci, G.; de Gironcoli, S.; Baroni, S. Electronic and Atomistic Structures of Clean and Reduced Ceria Surfaces. *J. Phys. Chem. B* **2005**, *109*, 22860.
- (107) Korotin, D.; Kozhevnikov, A. V.; Skornyakov, S. L.; Leonov, I.; Binggeli, N.; Anisimov, V. I.; Trimarchi, G. Construction and Solution of a Wannier-Functions Based Hamiltonian in the Pseudopotential Plane-Wave Framework for Strongly Correlated Materials. *Eur. Phys. J. B* **2008**, *65*, 91.
- (108) Ma, J.; Wang, L. W. Using Wannier Functions to Improve Solid Band Gap Predictions in Density Functional Theory. *Sci Rep-Uk* **2016**, *6*, 24924.
- (109) Larsen, A. H.; Mortensen, J. J.; Blomqvist, J.; Castelli, I. E.; Christensen, R.; Dulak, M.; Friis, J.; Groves, M. N.; Hammer, B.; Hargus, C. et al. The Atomic Simulation Environment—a Python Library for Working with Atoms. *J. Phys.: Condens. Matter* **2017**, *29*, 273002.
- (110) Hellenbrandt, M. The Inorganic Crystal Structure Database (Icsd)—Present and Future. *Crystallography Reviews* **2004**, *10*, 17.
- (111) Giannozzi, P.; Andreussi, O.; Brumme, T.; Bunau, O.; Nardelli, M. B.; Calandra, M.; Car, R.; Cavazzoni, C.; Ceresoli, D.; Cococcioni, M. et al. Advanced Capabilities for Materials Modelling with Quantum Espresso. *J. Phys.: Condens. Matter* **2017**, *29*, 465901.
- (112) Perdew, J. P.; Burke, K.; Ernzerhof, M. Generalized Gradient Approximation Made Simple. *Phys. Rev. Lett.* **1996**, *77*, 3865.
- (113) Rappe, A. M.; Rabe, K. M.; Kaxiras, E.; Joannopoulos, J. D. Optimized Pseudopotentials. *Phys. Rev. B* **1990**, *41*, 1227.
- (114) Vanderbilt, D. Soft Self-Consistent Pseudopotentials in a Generalized Eigenvalue Formalism. *Phys. Rev. B* **1990**, *41*, 7892.
- (115) <http://www.quantum-espresso.org/pseudopotentials>. (Accessed June 13, 2021).
- (116) Broyden, C. G. The Convergence of a Class of Double-Rank Minimization Algorithms 1. General Considerations. *IMA Journal of Applied Mathematics* **1970**, *6*, 76.
- (117) Broyden, C. G. The Convergence of a Class of Double-Rank Minimization Algorithms: 2. The New Algorithm. *IMA Journal of Applied Mathematics* **1970**, *6*, 222.
- (118) Fletcher, R. A New Approach to Variable Metric Algorithms. *Comput. J.* **1970**, *13*, 317.
- (119) Goldfarb, D. A Family of Variable-Metric Methods Derived by Variational Means. *Math. Comput.* **1970**, *24*, 23.
- (120) Shanno, D. F. Conditioning of Quasi-Newton Methods for Function Minimization. *Math. Comput.* **1970**, *24*, 647.

- (121) Marzari, N.; Mostofi, A. A.; Yates, J. R.; Souza, I.; Vanderbilt, D. Maximally Localized Wannier Functions: Theory and Applications. *Rev. Mod. Phys.* **2012**, *84*, 1419.
- (122) Momma, K.; Izumi, F. Vesta 3 for Three-Dimensional Visualization of Crystal, Volumetric and Morphology Data. *J. Appl. Crystallogr.* **2011**, *44*, 1272.
- (123) Lowdin, P. O. On the Non-Orthogonality Problem Connected with the Use of Atomic Wave Functions in the Theory of Molecules and Crystals. *J. Chem. Phys.* **1950**, *18*, 365.
- (124) Perera, U. G. E.; Kulik, H. J.; Iancu, V.; da Silva, L. G. G. V. D.; Ulloa, S. E.; Marzari, N.; Hla, S. W. Spatially Extended Kondo State in Magnetic Molecules Induced by Interfacial Charge Transfer. *Phys. Rev. Lett.* **2010**, *105*, 106601.
- (125) Rohrbach, A.; Hafner, J.; Kresse, G. Molecular Adsorption on the Surface of Strongly Correlated Transition-Metal Oxides: A Case Study for Co/NiO(100). *Phys. Rev. B* **2004**, *69*, 075413.
- (126) Morgan, B. J.; Watson, G. W. Polaronic Trapping of Electrons and Holes by Native Defects in Anatase TiO₂. *Phys. Rev. B* **2009**, *80*, 233102.
- (127) Kulik, H. J.; Seelam, N.; Mar, B. D.; Martinez, T. J. Adapting Dft Plus U for the Chemically Motivated Correction of Minimal Basis Set Incompleteness. *J. Phys. Chem. A* **2016**, *120*, 5939.
- (128) Meredig, B.; Thompson, A.; Hansen, H. A.; Wolverton, C.; van de Walle, A. Method for Locating Low-Energy Solutions within Dft Plus U. *Phys. Rev. B* **2010**, *82*, 195128.
- (129) Becke, A. D. Density-Functional Exchange-Energy Approximation with Correct Asymptotic-Behavior. *Phys. Rev. A* **1988**, *38*, 3098.
- (130) Lee, C. T.; Yang, W. T.; Parr, R. G. Development of the Colle-Salvetti Correlation-Energy Formula into a Functional of the Electron-Density. *Phys. Rev. B* **1988**, *37*, 785.
- (131) Perdew, J. P.; Ernzerhof, M.; Burke, K. Rationale for Mixing Exact Exchange with Density Functional Approximations. *J. Chem. Phys.* **1996**, *105*, 9982.
- (132) Adamo, C.; Barone, V. Toward Reliable Density Functional Methods without Adjustable Parameters: The Pbe0 Model. *J. Chem. Phys.* **1999**, *110*, 6158.

For Table of Contents Use Only



Supporting Information for

Eliminating Delocalization Error to Improve Heterogeneous Catalysis Predictions with Molecular DFT+U

Akash Bajaj^{1,2} and Heather J. Kulik¹

¹Department of Chemical Engineering, Massachusetts Institute of Technology, Cambridge, MA 02139

²Department of Materials Science and Engineering, Massachusetts Institute of Technology, Cambridge, MA 02139

Contents

Table S1 Lattice parameters of bulk rutile metal oxides with +U correction	Page S3
Table S2 DFT-relaxed metal–adsorbate (M–O*) bond lengths	Page S3
Figure S1 Structures of all PtO ₂ models	Page S4
Figure S2 Structures of all TiO ₂ models	Page S5
Table S3 List of pseudopotentials used	Page S5
Text S1 Construction of Wannier functions and using them as projectors within DFT+U	Page S6
Table S4 Total number of PBE-level eigenstates for TiO ₂ and PtO ₂	Page S7
Table S5 Comparison between geometry optimized and single-point surface energies	Page S7
Table S6 Grid resolutions of electron density cube files	Page S7
Table S7 DFT+U and Hartree–Fock exchange sensitivities of the surface energy	Page S8
Figure S3 Density difference between slab and bulk rutile TiO ₂ near the (110) plane	Page S9
Figure S4 Density difference between slab and bulk rutile VO ₂ near the (110) plane	Page S10
Figure S5 Density difference between slab and bulk rutile RuO ₂ near the (110) plane	Page S11
Figure S6 Density difference between slab and bulk rutile RhO ₂ near the (110) plane	Page S12
Figure S7 Density difference between slab and bulk rutile IrO ₂ near the (110) plane	Page S13
Figure S8 Density difference between slab and bulk rutile PtO ₂ near the (110) plane	Page S14
Figure S9 Representative schematic for integration of the absolute density difference	Page S15
Table S8 Integrals of the absolute density difference between slab and bulk MO ₂	Page S15
Table S9 DFT+U and Hartree–Fock exchange sensitivities of the adsorption energy	Page S16
Figure S10 Density difference between O*-adsorbed and pristine MO ₂ (110) slabs	Page S16
Table S10 Density difference along the M–O* bond after adsorption	Page S17
Table S11 Fractionalities and DFT+U sensitivities for 2D PtO ₂ exfoliation energy	Page S17
Table S12 AO contributions of candidate molecular projectors for 2D PtO ₂	Page S18
Table S13 Fractionalities and DFT+U sensitivities for 2D TiO ₂ adsorption energy	Page S19
Figure S11 Fractionality-based selection of molecular projectors for 2D TiO ₂	Page S19
Figure S12 Projected density of states for pristine and decorated 2D TiO ₂	Page S20
Table S14 AO contributions of candidate molecular projectors for pristine 2D TiO ₂	Page S21
Table S15 AO contributions of candidate molecular projectors for decorated 2D TiO ₂	Page S22
Figure S13 Projected density of states for bulk rutile PtO ₂	Page S23
Figure S14 Projected density of states for pristine PtO ₂ (110)	Page S23
Figure S15 Projected density of states for O*-adsorbed PtO ₂ (110)	Page S24

Table S16 AO contributions of molecular projectors for pristine PtO ₂ (110)	Page S25
Table S17 AO contributions of molecular projectors for O*-adsorbed PtO ₂ (110)	Page S26
Table S18 AO contributions of molecular projectors for pristine TiO ₂ (110)	Page S27
Table S19 AO contributions of molecular projectors for O*-adsorbed TiO ₂ (110)	Page S28
Figure S16 DFT+U sensitivities and PDOS using fixed pristine MOPs for PtO ₂	Page S29
Figure S17 DFT+U sensitivities and PDOS using fixed pristine MOPs for TiO ₂	Page S30
References	Page S30

Table S1. Experimental and geometry-optimized lattice parameters a and c (in Å) of bulk rutile transition metal oxides MO_2 ($M = \text{Ti, V, Ru, Rh, Ir, Pt}$) with U (in eV) for DFT+U.

M		expt.	PBE	1 eV	2 eV	3 eV	4 eV	5 eV	6 eV	7 eV	8 eV	9 eV	10 eV
Ti	a	4.594	4.619	4.622	4.625	4.628	4.631	4.635	4.640	4.647	4.655	4.663	4.674
	c	2.959	2.956	2.970	2.986	3.001	3.019	3.037	3.056	3.077	3.097	3.118	3.138
V	a	4.555	4.612	4.615	4.620	4.632	4.651	4.663	4.674	4.687	4.701	4.720	4.741
	c	2.853	2.778	2.779	2.777	2.766	2.755	2.765	2.770	2.777	2.787	2.799	2.817
Ru	a	4.492	4.649	4.641	4.634	4.629	4.625	4.623	4.621	4.620	4.619	4.621	4.621
	c	3.107	3.190	3.191	3.193	3.193	3.194	3.192	3.191	3.190	3.190	3.188	3.188
Rh	a	4.489	4.632	4.631	4.631	4.632	4.633	4.634	4.636	4.638	4.639	4.641	4.642
	c	3.090	3.174	3.172	3.170	3.168	3.167	3.166	3.165	3.164	3.163	3.163	3.163
Ir	a	4.505	4.590	4.589	4.588	4.588	4.587	4.587	4.588	4.588	4.589	4.589	4.590
	c	3.159	3.214	3.211	3.208	3.205	3.202	3.200	3.197	3.195	3.193	3.191	3.189
Pt	a	4.485	4.642	4.642	4.641	4.640	4.639	4.639	4.639	4.638	4.638	4.637	4.637
	c	3.130	3.280	3.275	3.271	3.268	3.265	3.264	3.262	3.262	3.262	3.263	3.264

Table S2. Geometry-optimized bond lengths between metal adsorption site and O-atom adsorbate (in Å) at the DFT level for the (110) surface of rutile transition metal oxides MO_2 ($M = \text{Ti, V, Ru, Rh, Ir, Pt}$). Initial bond lengths were specified using the DFT-level optimized values obtained from Ref. [1] to provide a better initial guess.

M	Initial	PBE
Ti	1.676	1.672
V	1.589	1.589
Ru	1.809	1.809
Rh	1.825	1.823
Ir	1.814	1.813
Pt	1.862	1.859
2D Ti	1.676	1.637

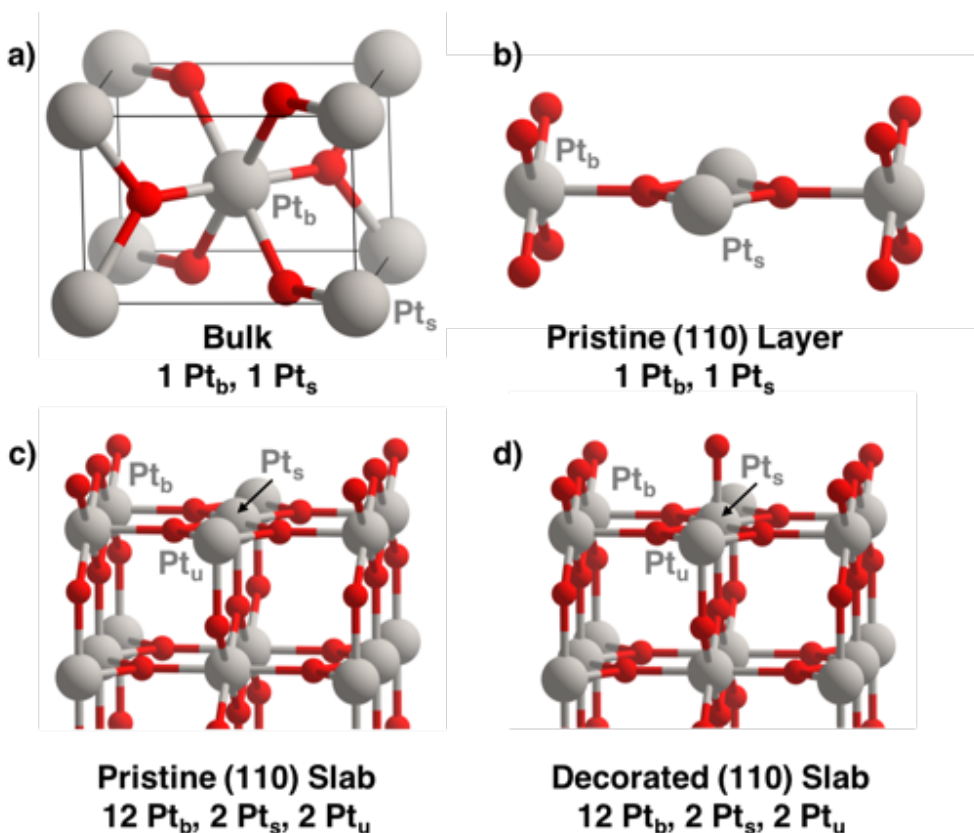


Figure S1. Structures of the a) bulk rutile, b) pristine 2D, c) pristine slab, and d) decorated slab models of rutile PtO₂. Pt atoms are indicated using gray spheres and oxygen atoms are indicated using red spheres. Pt sites are identified using two or three different types for all DFT+U calculations, where ‘Pt_b’ indicates a bulk-like fully coordinated site, ‘Pt_u’ indicates a surface undercoordinated site and ‘Pt_s’ indicates the site of adsorption. The number of each site within a unit cell is annotated. Note that Pt_s and Pt_u are otherwise equivalent for all pristine surface models.

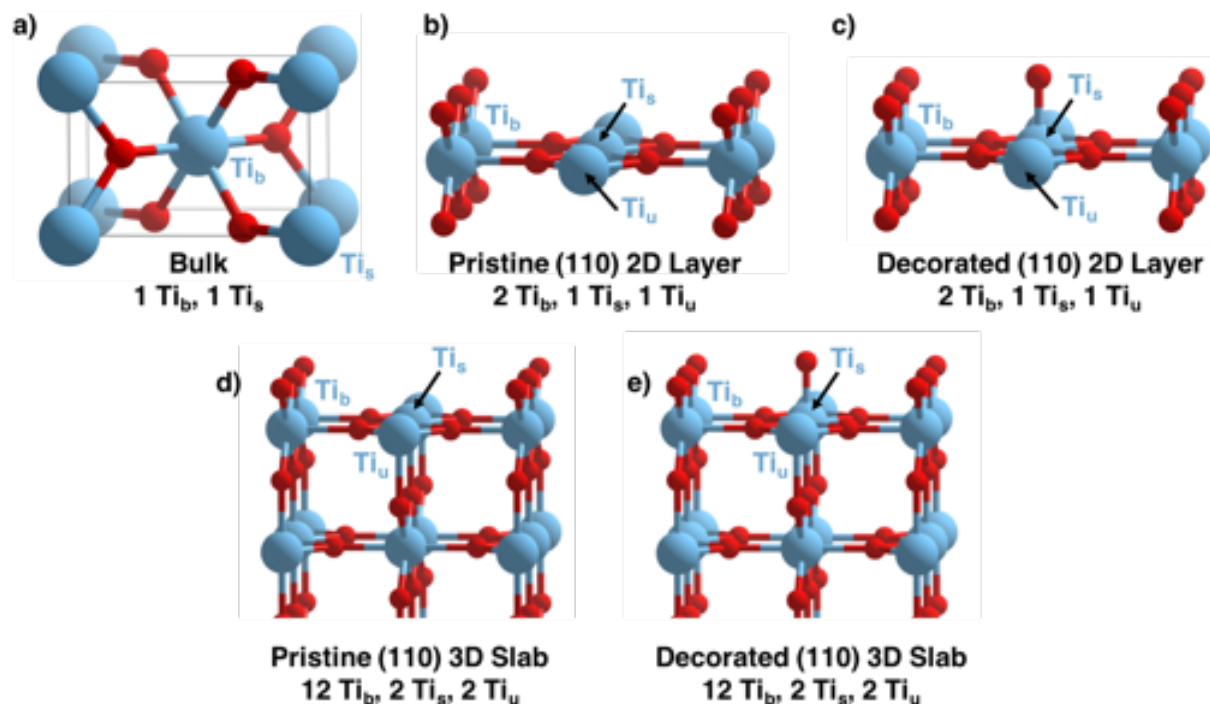


Figure S2. Structures of the a) bulk rutile, b) pristine 2D, c) decorated 2D, d) pristine slab and d) decorated slab models of rutile TiO₂. Ti atoms are indicated using blue spheres and oxygen atoms are indicated using red spheres. Ti sites are identified using three different types for all DFT+U calculations, where ‘Ti_b’ indicates a bulk-like fully coordinated site, ‘Ti_u’ indicates a surface undercoordinated site and ‘Ti_s’ indicates the site of adsorption. The number of each site within a unit cell is annotated. Note that Ti_s and Ti_u are otherwise equivalent for all pristine surface models.

Table S3. List of all pseudopotentials employed in this work with filenames identical to those obtained from the Quantum-ESPRESSO website². The valence electrons that are explicitly modeled are indicated with any semi-core states underlined where applicable.

Element	Pseudopotential Name	Valence States
Ti	Ti.pbe-sp-van_ak.UPF	<u>3s</u> , <u>3p</u> , 3d, 4s
V	V.pbe-sp-van.UPF	<u>3s</u> , <u>3p</u> , 3d, 4s, 4p
Ru	Ru.pbe-n-van.UPF	4d, 5s, 5p
Rh	Rh.pbe-rrkjus.UPF	4d, 5s
Ir	Ir.pbe-n-rrkjus.UPF	5d, 6s, 6p
Pt	Pt.pbe-n-van.UPF	5d, 6s, 6p
O	O.pbe-van_ak.UPF	2s, 2p

Text S1. Construction of Wannier functions and their use as projectors within DFT+U

The transformation of plane-wave eigenstates $|\psi_{\mathbf{k},\nu}\rangle$, where \mathbf{k} denotes the k -point and ν denotes the band index, to Wannier functions was carried out using the **pmw.x** utility available with the Quantum-ESPRESSO package³. From the total number of available eigenstates, we select a specific set by providing a contiguous range for the band index i.e., ν_i to ν_f . The procedure followed by **pmw.x** after providing it with this selection is as follows:

The selected plane-wave states $\{|\psi_{\mathbf{k},\nu}\rangle\}$ are first projected on the atomic orbitals (AOs) $\{|\phi_{\lambda'}^I\rangle\}$ localized on a Hubbard site I :

$$|\tilde{\psi}_{\mathbf{k},\lambda'}^I\rangle = \sum_{\nu=\nu_i}^{\nu_f} |\psi_{\mathbf{k},\nu}\rangle \langle \psi_{\mathbf{k},\nu} | \phi_{\lambda'}^I \rangle, \quad (1)$$

to obtain a set of transformed states $\{|\tilde{\psi}_{\mathbf{k},\lambda'}^I\rangle\}$ corresponding to each Hubbard site I . For our transition metal oxides, the AOs were the five valence d atomic orbitals of the Hubbard metal site(s), obtained from the all-electron calculation carried out for pseudopotential generation.

The transformed states are then orthonormalized using the Löwdin symmetric orthonormalization procedure:

$$|\bar{\psi}_{\mathbf{k},\lambda}^I\rangle = \sum_{\lambda'} |\tilde{\psi}_{\mathbf{k},\lambda'}^I\rangle (S_{\mathbf{k}}^{-1/2})_{\lambda'\lambda}, \quad (2)$$

where $S_{\mathbf{k}}$, the overlap matrix, is defined as $(S_{\mathbf{k}})_{\lambda'\lambda} = \langle \tilde{\psi}_{\mathbf{k},\lambda'}^I | \tilde{\psi}_{\mathbf{k},\lambda}^I \rangle$. The normalized states $\{|\bar{\psi}_{\mathbf{k},\lambda}^I\rangle\}$ are then Fourier transformed from their \mathbf{k} -space representation to their real-space representation to obtain the desired Wannier functions for the corresponding Hubbard site I :

$$|\mathbf{R}_{\lambda}^I\rangle = \frac{V}{(2\pi)^3} \int_{\text{BZ}} d\mathbf{k} e^{-i\mathbf{k}\cdot\mathbf{R}} |\bar{\psi}_{\mathbf{k},\lambda}^I\rangle, \quad (3)$$

where V represents the volume of the primitive unit cell in real space.

The generated Wannier functions are used as projectors using the `u_projection_type = 'file'` command within a DFT+U calculation in Quantum-ESPRESSO, whereupon they replace the AO projectors for only the aforementioned Hubbard site(s) I .

Table S4. Total number of eigenstates $|\psi_{\mathbf{k},v}\rangle$ generated per \mathbf{k} -point at the PBE level as specified using the nbnd keyword within Quantum-ESPRESSO for different models of TiO₂ and PtO₂. “Decorated” refers to a surface model with 0.5 monolayer coverage of oxygen adatoms whereas “pristine” refers to the surface model without the oxygen adatoms.

Structure	Geometry Model	Total Number of States
TiO ₂	Bulk Rutile	50
	Pristine (110) 3D Slab	250
	Pristine (110) 2D Layer	75
	Decorated (110) 3D Slab	250
	Decorated (110) 2D Layer	75
PtO ₂	Bulk Rutile	50
	Pristine (110) 3D Slab	250
	Pristine (110) 2D Layer	50
	Decorated (110) 3D Slab	250

Table S5. Comparison of DFT+U surface formation energies, E_σ (eV/(110) u.a.), for the (110) surface of rutile TiO₂ evaluated using optimized geometries at each U and using the DFT-level (i.e. $U = 0$ eV) geometry with single-point energy calculations at each U . All calculations employed a Hubbard U on all Ti sites and were carried out using Ti(3d) atomic orbitals as the projector basis within DFT+U.

U value (eV)	E_σ from geometry optimizations	E_σ from single-point energies using DFT-level geometry
0	0.77	0.77
1	0.82	0.81
2	0.87	0.85
3	0.92	0.90
4	0.98	0.95
5	1.05	1.00

Table S6. Grid resolutions, i.e., the number of grid points along each axis, used to generate electron density cube files of bulk and slab models of rutile transition metal oxides, MO₂.

M	Geometry Model(s)	x Grid Points	y Grid Points	z Grid Points
Ti	Bulk Rutile	200	200	133
	3D Slabs	200	266	321
V	Bulk Rutile	200	200	200
	3D Slabs	200	400	311
Ru	Bulk Rutile	200	200	200
	3D Slabs	200	400	328
Rh	Bulk Rutile	200	200	200
	3D Slabs	200	400	312
Ir	Bulk Rutile	200	200	200
	3D Slabs	200	400	327
Pt	Bulk Rutile	200	200	148
	3D Slabs	200	296	325

Table S7. Linearized sensitivity of the surface formation energy, $S(E_\sigma)$, for the (110) planes of rutile transition metal oxides, MO_2 . The sensitivities are computed with respect to the U value (in eV/(110) u.a. per eV of U) using PBE+U in a plane-wave basis set (and multiplied by 10) or obtained from Ref. [1] (in eV/(110) u.a. per HFX) where it was computed with respect to a change in Hartree–Fock (HF) exchange fraction, a_{HF} , from 0 to 1 (i.e., 1 HFX) in the PBE0⁴⁻⁶ global hybrid functional using an atom-centered basis set. The DFT+U sensitivity for VO_2 was obtained from Ref. [1].

M	DFT+U $S(E_\sigma)$ (10×) (eV (110)u.a.⁻¹ eV⁻¹)	a_{HF} $S(E_\sigma)$ (eV (110)u.a.⁻¹ HFX⁻¹)
Ti	0.66	0.95
V	0.44	0.74
Ru	0.39	3.00
Rh	0.05	1.31
Ir	0.14	0.67
Pt	0.04	3.90

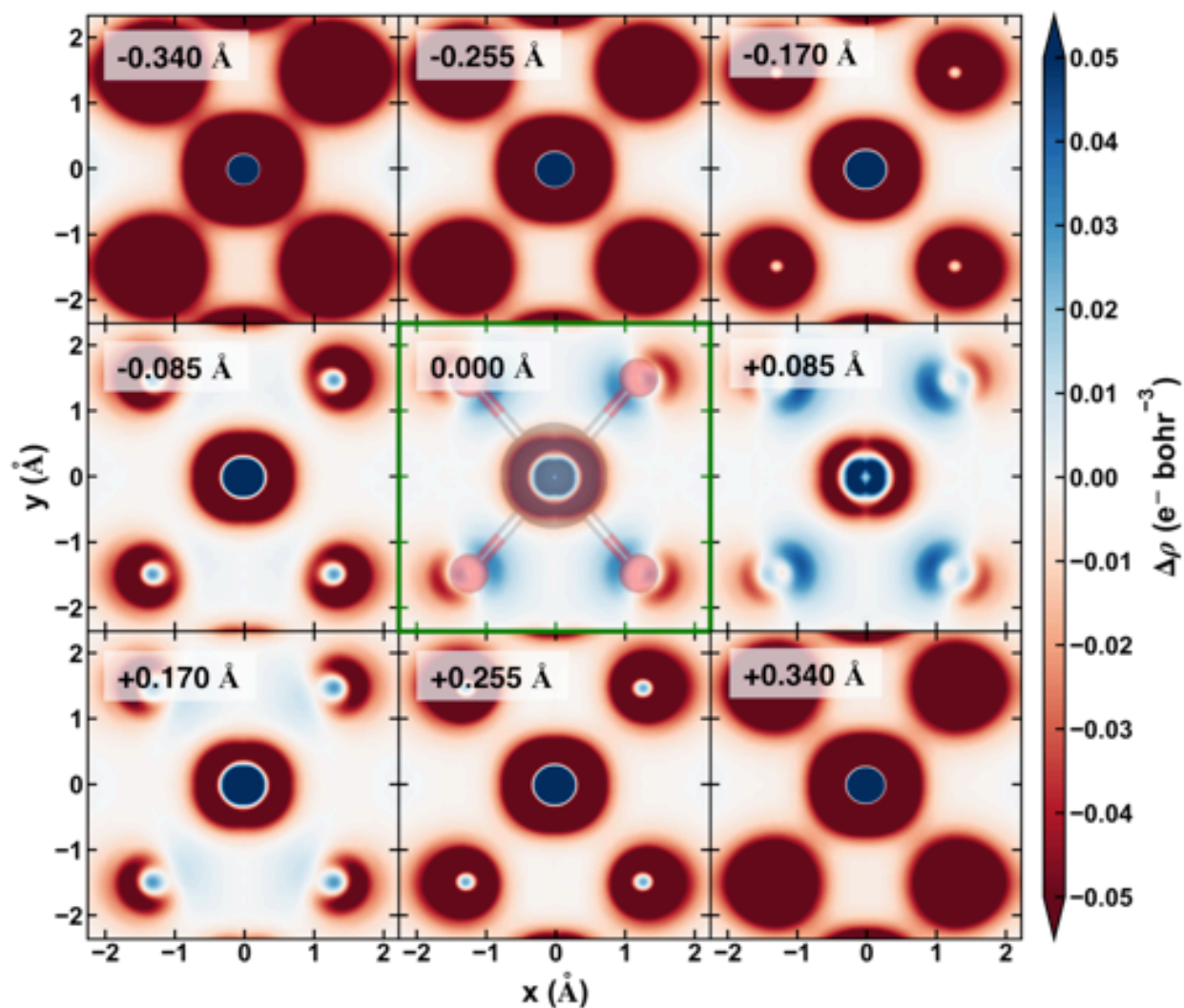


Figure S3. Density difference, $\Delta\rho$, between the pristine slab and the bulk rutile model of TiO₂ computed for the (110) plane (middle pane, outlined in green with atom positions shown) and at vertical distances ranging from below the (110) plane ($z = 0$ Å) at -0.34 Å to above at $+0.34$ Å as annotated in inset. Red indicates density loss and blue indicates density gain after the surface has been cleaved.

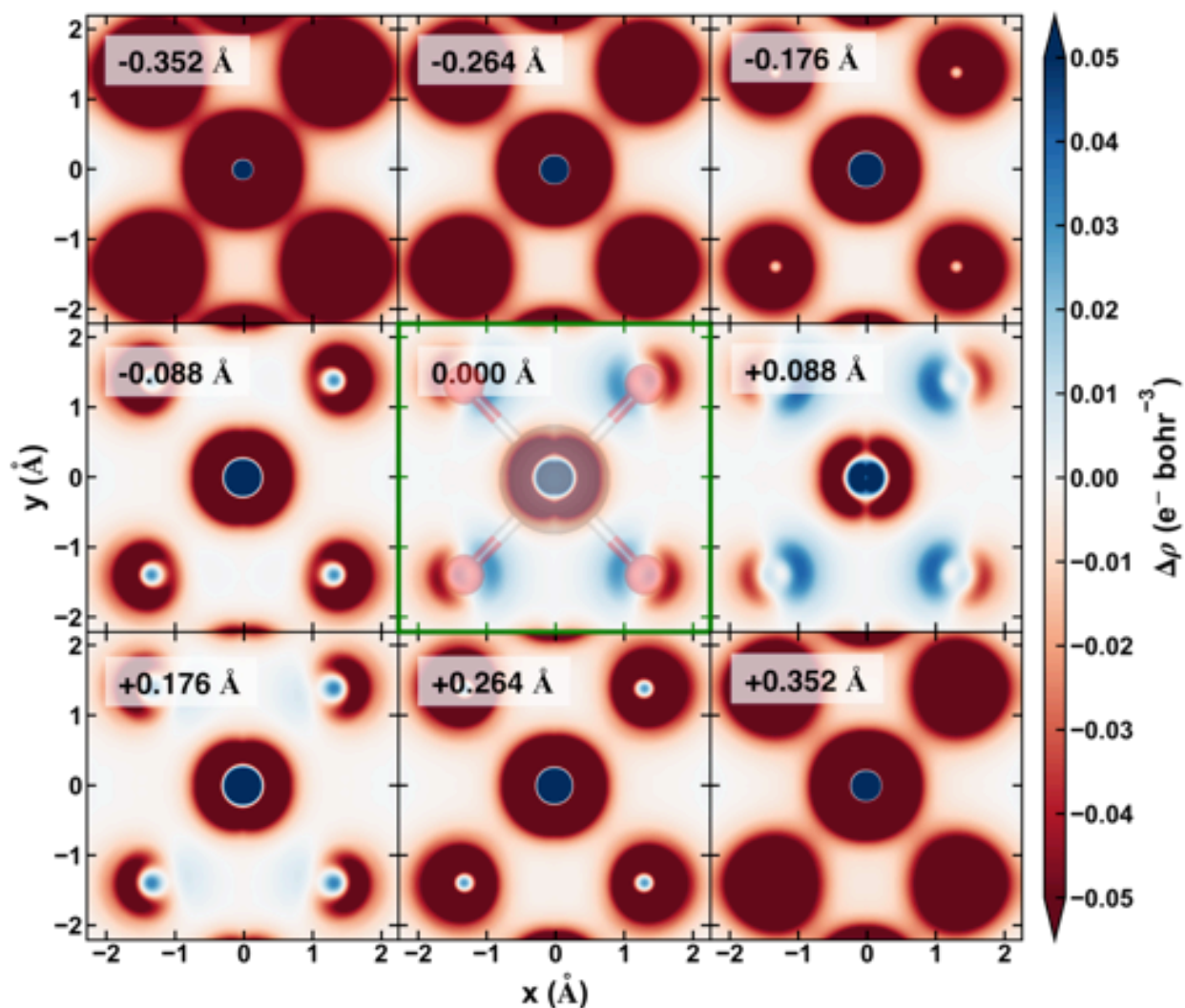


Figure S4. Density difference, $\Delta\rho$, between the pristine slab and the bulk rutile model of VO_2 computed for the (110) plane (middle pane, outlined in green with atom positions shown) and at vertical distances ranging from below the (110) plane ($z = 0 \text{ \AA}$) at -0.352 \AA to above at $+0.352 \text{ \AA}$ as annotated in inset. Red indicates density loss and blue indicates density gain after the surface has been cleaved.

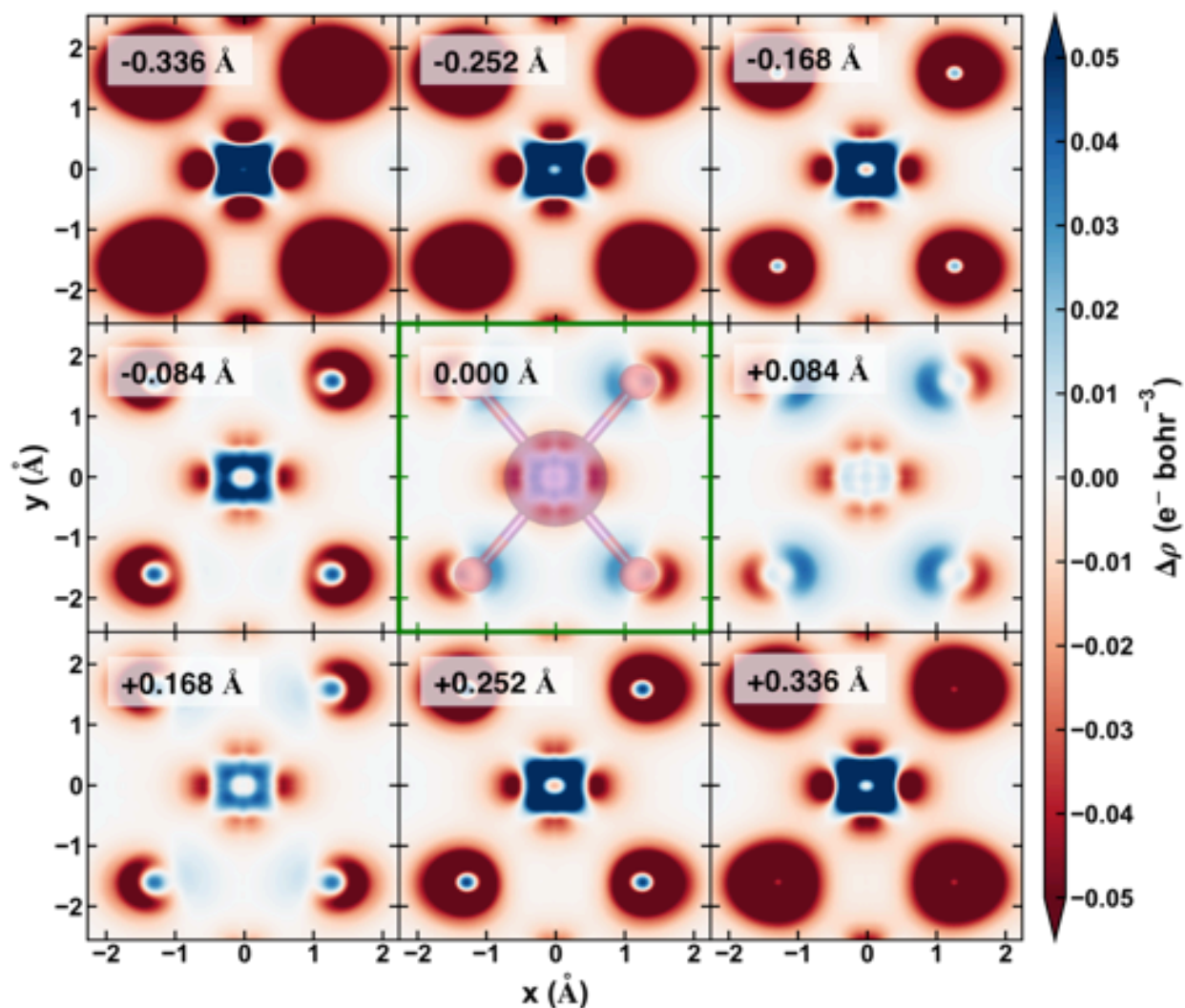


Figure S5. Density difference, $\Delta\rho$, between the pristine slab and the bulk rutile model of RuO_2 computed for the (110) plane (middle pane, outlined in green with atom positions shown) and at vertical distances ranging from below the (110) plane ($z = 0$ Å) at -0.336 Å to above at $+0.336$ Å as annotated in inset. Red indicates density loss and blue indicates density gain after the surface has been cleaved.

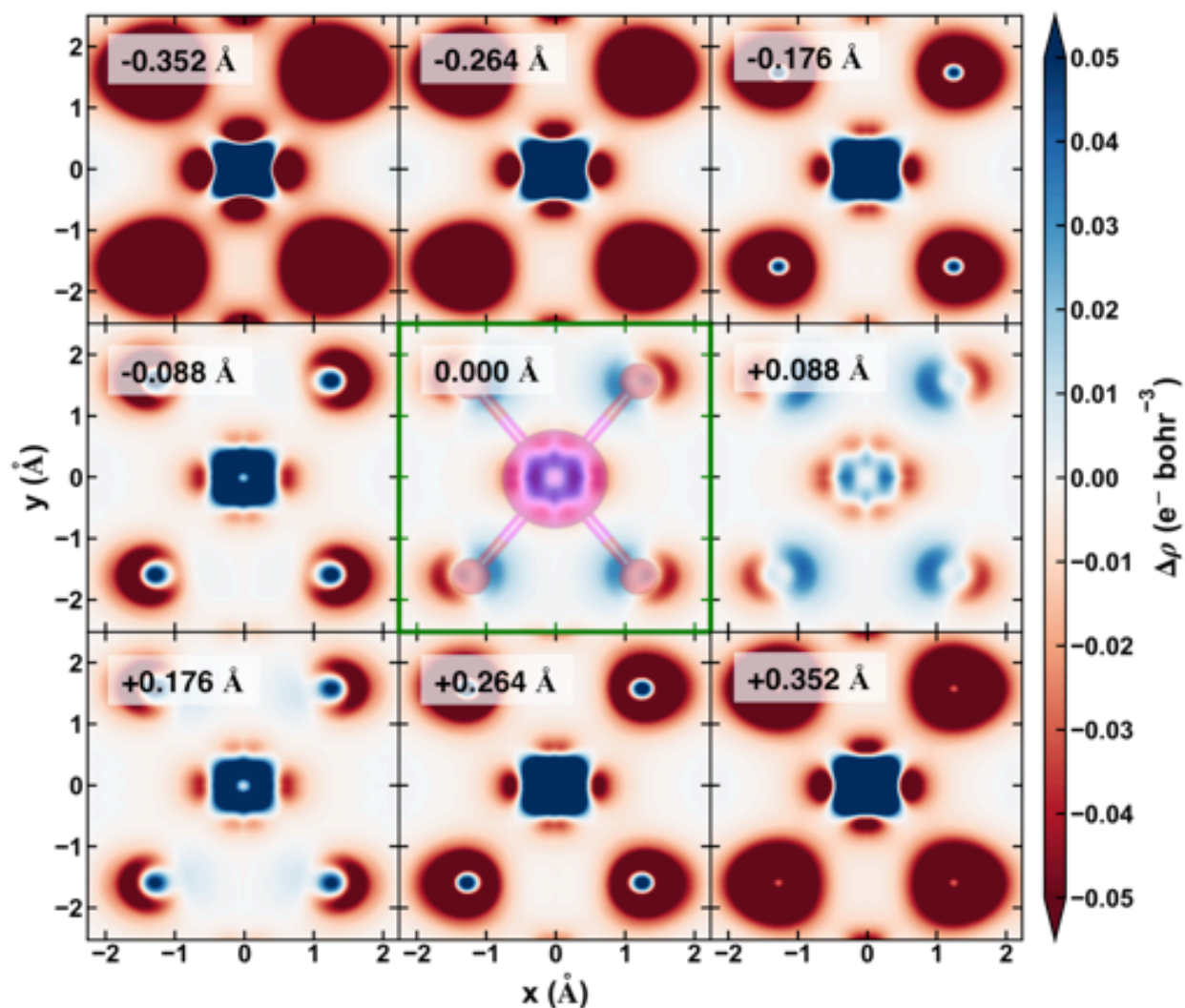


Figure S6. Density difference, $\Delta\rho$, between the pristine slab and the bulk rutile model of RhO_2 computed for the (110) plane (middle pane, outlined in green with atom positions shown) and at vertical distances ranging from below the (110) plane ($z = 0$ Å) at -0.352 Å to above at $+0.352$ Å as annotated in inset. Red indicates density loss and blue indicates density gain after the surface has been cleaved.

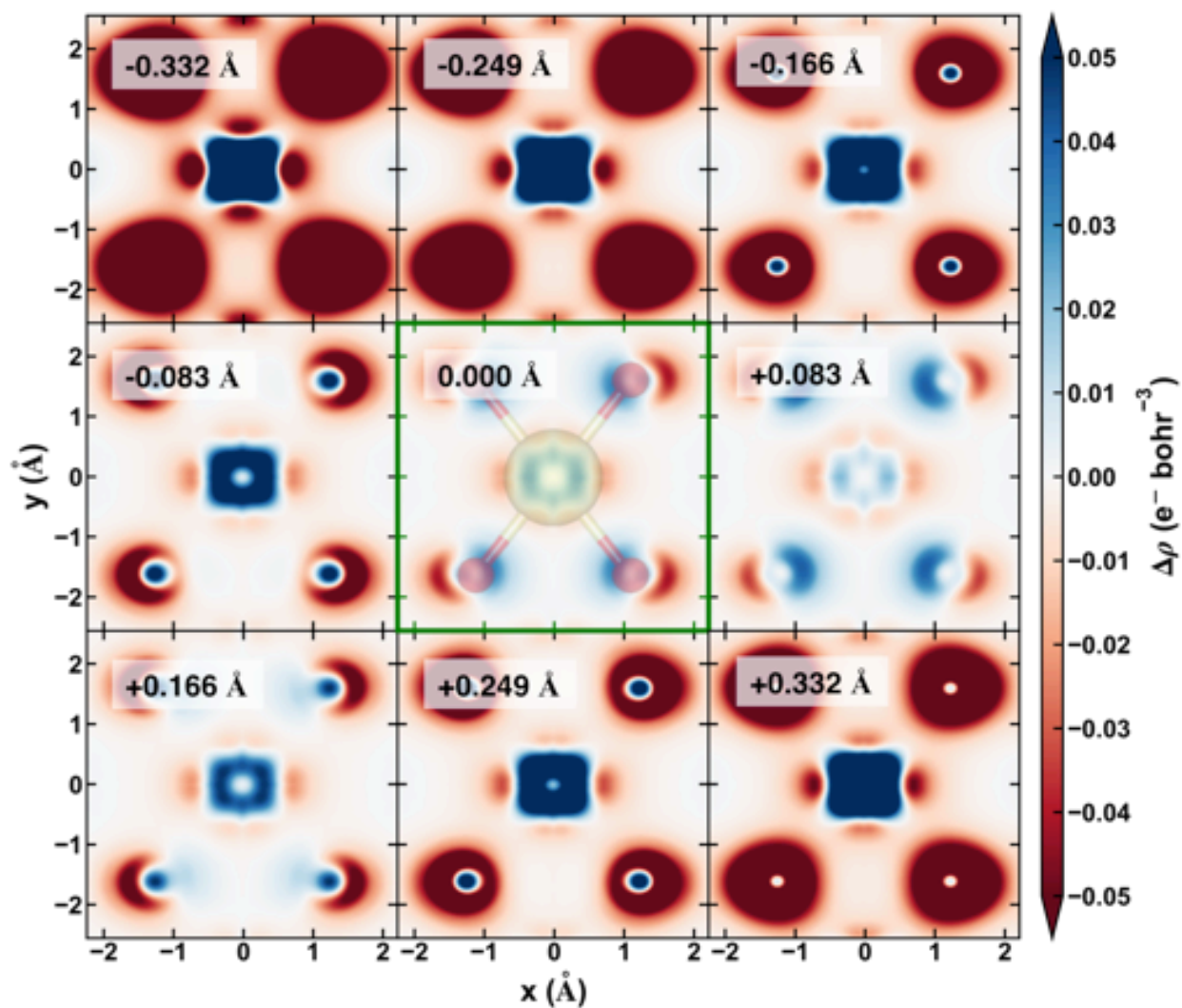


Figure S7. Density difference, $\Delta\rho$, between the pristine slab and the bulk rutile model of IrO₂ computed for the (110) plane (middle pane, outlined in green with atom positions shown) and at vertical distances ranging from below the (110) plane ($z = 0$ Å) at -0.332 Å to above at $+0.332$ Å as annotated in inset. Red indicates density loss and blue indicates density gain after the surface has been cleaved.

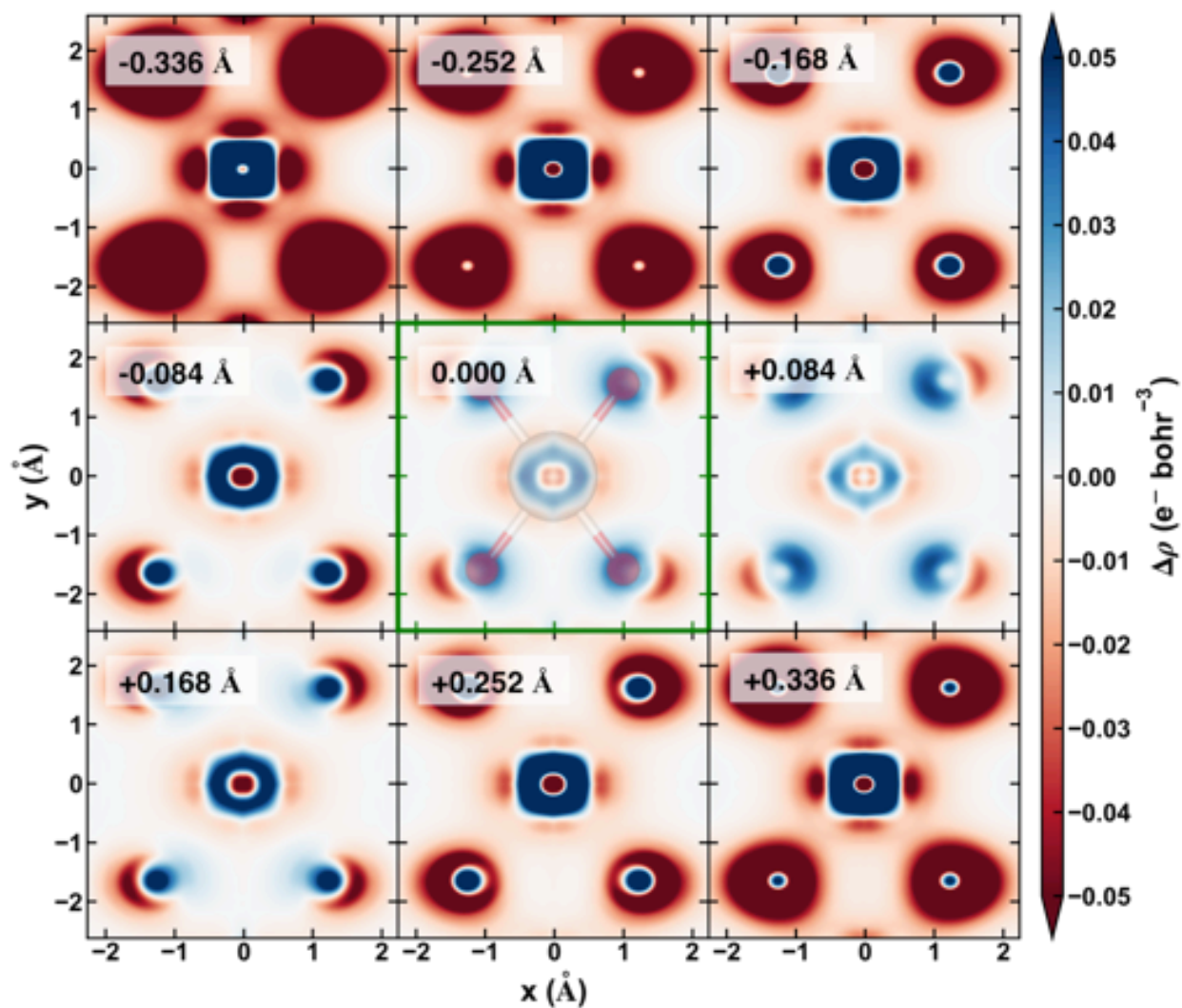


Figure S8. Density difference, $\Delta\rho$, between the pristine slab and the bulk rutile model of PtO_2 computed for the (110) plane (middle pane, outlined in green with atom positions shown) and at vertical distances ranging from below the (110) plane ($z = 0$ Å) at -0.336 Å to above at $+0.336$ Å as annotated in inset. Red indicates density loss and blue indicates density gain after the surface has been cleaved.

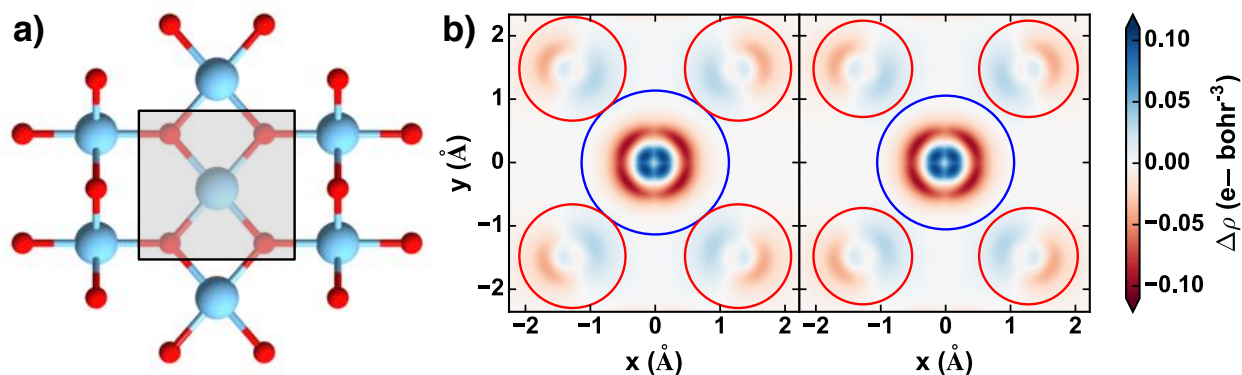


Figure S9. (a) Top view of the $\text{TiO}_2(110)$ surface plane with Ti in blue and O in red. (b) Density difference, $\Delta\rho$, between the pristine slab and the bulk rutile models of TiO_2 computed within the shaded region of the (110) plane indicated in (a). The integration of $|\Delta\rho|$ is evaluated within a circular region around the metal (blue circles) and around the oxygen (red circles). The radii of the circles were computed either by scaling down the van der Waals radii⁷ of each atom such that the metal and oxygen circles touched (left pane) or by scaling the van der Waals radii⁷ of each atom by 0.5x (right pane) to keep a consistent O atom radius for all metals.

Table S8. Integral of $|\Delta\rho|$ for $\text{MO}_2(110)$ surface formation within a circular region centered at the metal site and the sum over all oxygen atoms. All integral values are reported in units of e-bohr with the fraction of the integral value at the metal site indicated separately. The radii of the circular regions for integration were obtained after scaling the van-der Waals radii⁷ of the metal and oxygen atoms, (i) by a system-dependent ‘variable scale factor’ such that the metal- and oxygen-centered circles touched, and (ii) by a ‘fixed scale factor’ of 0.5x.

MO_2	<u>Variable scale factor</u>			<u>Fixed scale factor</u>		
	Metal	Oxygen (total)	Metal contribution	Metal	Oxygen (total)	Metal contribution
TiO_2	0.3790	0.3955	48.9%	0.3741	0.3661	50.5%
VO_2	0.4374	0.3837	53.3%	0.4349	0.3639	54.4%
RuO_2	0.1299	0.4021	24.4%	0.1229	0.3688	25.0%
RhO_2	0.1562	0.4067	27.8%	0.1508	0.3750	28.7%
IrO_2	0.1080	0.3946	21.5%	0.1014	0.3646	21.8%
PtO_2	0.1338	0.4358	23.5%	0.1266	0.4038	23.9%

Table S9. Linearized sensitivity of the adsorption energy, $S(\Delta E_o)$, for adsorption of 0.5 monolayer of O atoms on the (110) planes of rutile transition metal oxides, MO_2 . The sensitivities are computed with respect to the U value (in eV/eV of U) using PBE+ U in a plane-wave basis set (x10) or obtained from Ref. [1] (in eV/HFX) where it was computed with respect to a change in Hartree–Fock (HF) exchange fraction, a_{HF} , from 0 to 1 (i.e., 1 HFX) in the PBE0⁴⁻⁶ global hybrid functional using an atom-centered basis set.

M	DFT+ U $S(\Delta E_o)$ (10×) (eV/eV of U)	a_{HF} $S(\Delta E_o)$ (eV/HFX)
Ti	0.03	11.46
V	0.00	1.96
Ru	0.49	3.21
Rh	0.64	5.88
Ir	0.91	4.38
Pt	0.56	4.58

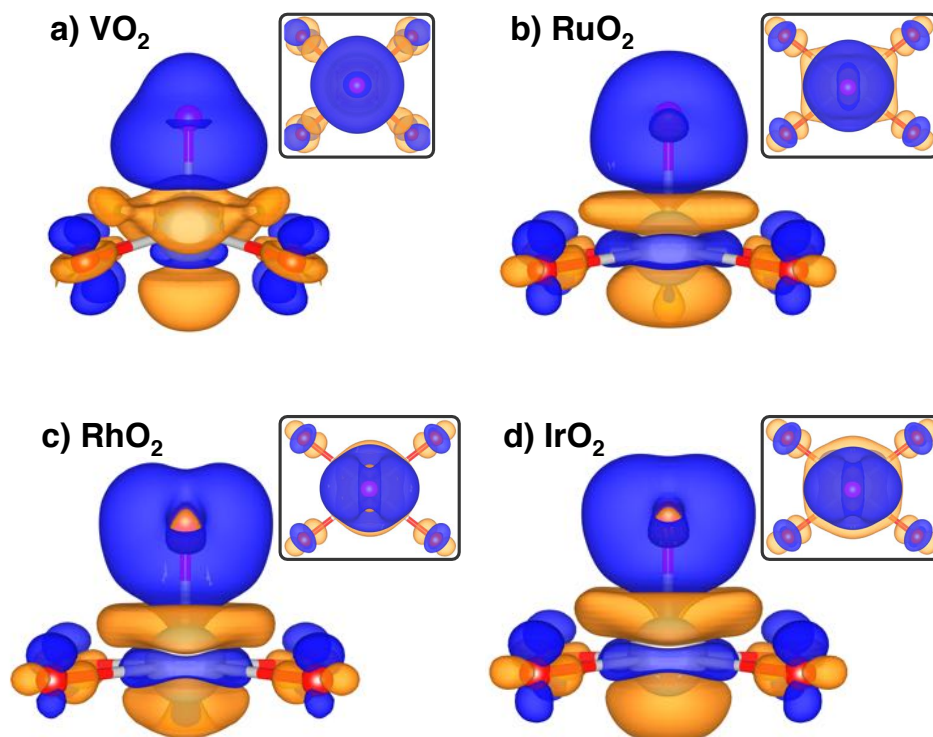


Figure S10. Isosurfaces for the density difference (isovalue: 0.003 e⁻/bohr³) between O*-adsorbed and pristine (110) surfaces of (a) VO₂, (b) RuO₂, (c) RhO₂ and (d) IrO₂. The metal adsorption site (gray spheres), the four in-plane coordinating O atoms (red spheres) and the O* adsorbate (pink spheres) are indicated in the front view with the top view depicted in the inset. Orange indicates density loss and blue indicates density addition after O* adsorption.

Table S10. Maximum absolute value of the density difference i.e., $|\Delta\rho|_{\max}$ (in $\text{e}^-/\text{\AA}^3$), between the O*-adsorbed and pristine $\text{MO}_2(110)$ surfaces evaluated along the M–O* bond.

M	$\Delta\rho _{\max}$ ($\text{e}^-/\text{\AA}^3$)
Ti	0.11
V	0.19
Ru	0.05
Rh	0.07
Ir	0.07
Pt	0.06

Table S11. Fractionality difference per orbital, $\Delta\text{Tr}[\mathbf{n}(1-\mathbf{n})]$ (in e^-^2), between 2D $\text{PtO}_2(110)$ and bulk rutile PtO_2 computed after summing over both unique Pt sites. $\Delta\text{Tr}[\mathbf{n}(1-\mathbf{n})]$ was computed at the PBE level of theory (i.e., $U = 0$ eV) using atomic projectors at both Pt sites (“Atomic”) or after replacing the atomic projectors at the undercoordinated Pt site, Pt_s , with fractionality-selected best molecular projectors constructed using the Wannier localization scheme, while retaining atomic projectors at the other Pt site (“Molecular”). Linearized sensitivities of the 2D PtO_2 exfoliation energy, $S(E_\sigma)$, computed with respect to the U value (in $\text{eV}/(110)\text{u.a.}$ per eV of U) using PBE+ U in a plane-wave basis set (and multiplied by 10) is also tabulated for each projector choice. As expected, the magnitude of ΔTr correlates strongly with the magnitude of $S(E_\sigma)$, validating our first-order approximation. However, the sign of the ΔTr does not correlate with that of $S(E_\sigma)$ for the atomic projections. This is because the ΔTr is too close to zero at $U = 0$ and we noticed a small decrease in ΔTr with increasing U , which will not be captured within this first-order approximation.

Projector Type	$\Delta\text{Tr}[\mathbf{n}(1-\mathbf{n})]$ (e^-^2)	DFT+U $S(E_\sigma)$ ($10\times$) ($\text{eV}(110)\text{u.a.}^{-1}\text{eV}^{-1}$)
Atomic	0.001	-0.13
Molecular	0.088	2.96

Table S12. Atomic orbital (AO) contributions from the Pt_s(5*d*) and O(2*p*) orbitals for all plane-wave states (i.e., “molecular orbitals”, labeled by their band index) available for Wannier function construction in 2D PtO₂ (110). All AO contributions are computed at the Γ -point using their projections on the AOs and are listed as a percentage. Pt(5*d*) and O(2*p*) columns show the sum of contributions from all the individual *d* and *p* AOs respectively. O(2*p_z*) AO contributions are listed separately. The five contiguous states used for constructing molecular projectors within the Wannier localization scheme are indicated in bold.

Band Index	Pt _s (5 <i>d</i>) (%)	O(2 <i>p</i>) (%)	O(2 <i>p_z</i>) (%)	Band Index	Pt _s (5 <i>d</i>) (%)	O(2 <i>p</i>) (%)	O(2 <i>p_z</i>) (%)
1	5.1	0.6	0.2	26	0	60.4	0
2	0	0	0	27	7.2	18.8	10.2
3	0.2	2.6	2.2	28	0	9.6	9.6
4	0	0.4	0.4	29	0.3	0.8	0.2
5	19.7	54.8	0	30	0	1	1
6	47.5	47.4	0	31	1.2	3	0
7	0	39.4	0	32	2.2	16.2	4.2
8	0.5	40.2	40.2	33	0	8.8	0
9	12	42.8	30.4	34	0	0.8	0.8
10	0	96	0	35	0.2	0	0
11	0	90	0	36	0.2	0.6	0
12	0	89.6	89.6	37	0	0.4	0
13	7.2	0	0	38	0	0.4	0.4
14	42	29.4	19.6	39	0	0.4	0.4
15	64	0.6	0	40	0	0	0
16	0	96.8	0	41	0	0.2	0
17	99.9	0	0	42	0	1	0.4
18	0	94.6	0	43	0.1	0	0
19	66.7	5.2	4.6	44	0	0	0
20	28.7	24.6	18	45	0	0	0
21	0	97	97	46	0	0	0
22	20.6	73.2	20.2	47	0	0	0
23	24.9	54.4	29.8	48	0	0.2	0.2
24	2.5	28.6	18.4	49	0.1	0	0
25	44.5	52	0	50	0	4.8	0

Table S13. Fractionality difference per orbital, $\Delta\text{Tr}[\mathbf{n}(1-\mathbf{n})]$ (in e^-^2), between pristine and O*-decorated 2D $\text{TiO}_2(110)$ computed after summing over all three unique Ti sites. $\Delta\text{Tr}[\mathbf{n}(1-\mathbf{n})]$ was computed at the PBE level of theory (i.e., $U = 0$ eV) using atomic projectors at all three Ti sites (“Atomic”), or after replacing the atomic projectors at the site of adsorption, Ti_s , with molecular projectors constructed using the Wannier localization scheme while retaining atomic projectors at the other two Ti sites. Molecular projectors were selected based on the maximum reported ΔTr (“Molecular, $\Delta\text{Tr}_{\text{max}}$ ”) or based on physical justification but with a relatively lower ΔTr (“Molecular, Alt.”). Linearized sensitivities of the adsorption energy of 0.5 monolayer of O atoms on 2D $\text{TiO}_2(110)$, $S(\Delta E_O)$, computed with respect to the U value (in eV per eV of U) using PBE+ U in a plane-wave basis set (and multiplied by 10) is also indicated for each projector choice.

Projector Type	$\Delta\text{Tr}[\mathbf{n}(1-\mathbf{n})]$ (e^-^2)	DFT+U $S(\Delta E_O)$ ($10\times$) (eV eV^{-1})
Atomic	0.006	-0.06
Molecular, $\Delta\text{Tr}_{\text{max}}$	0.031	5.08
Molecular, Alt.	0.010	4.40

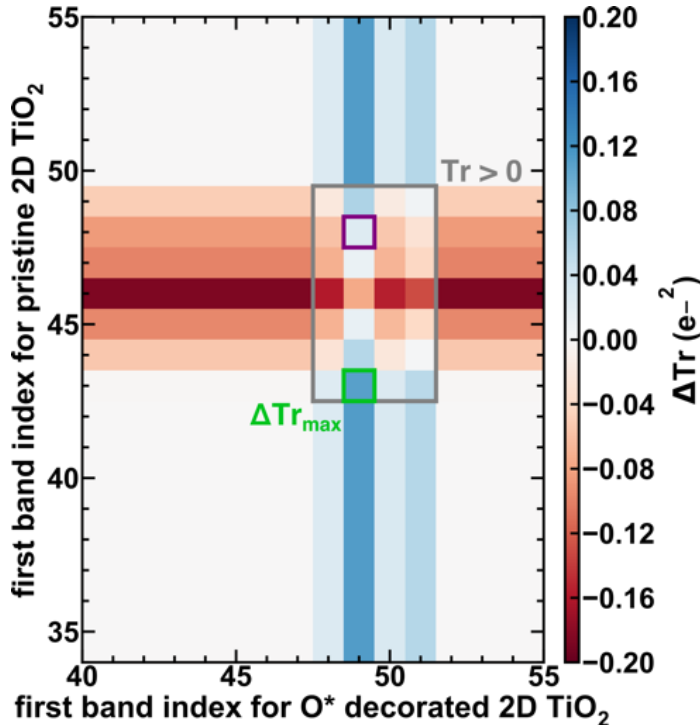


Figure S11. Fractionality difference per orbital, $\Delta\text{Tr}[\mathbf{n}(1-\mathbf{n})]$ (in e^-^2), between O*-decorated and pristine 2D $\text{TiO}_2(110)$ shown for representative molecular projectors constructed using the Wannier localization scheme for both systems. The index of the first band selected for the Wannier localization in O*-decorated 2D TiO_2 is shown on the x-axis and the index of the first band selected for the Wannier localization in pristine 2D TiO_2 is shown on the y-axis. The projector pair having the maximum $\Delta\text{Tr}[\mathbf{n}(1-\mathbf{n})]$ (green square) from those having a positive Tr (gray rectangle) is highlighted along with an alternative projector pair selected based on physical justification but having relatively lower $\Delta\text{Tr}[\mathbf{n}(1-\mathbf{n})]$ (purple square).

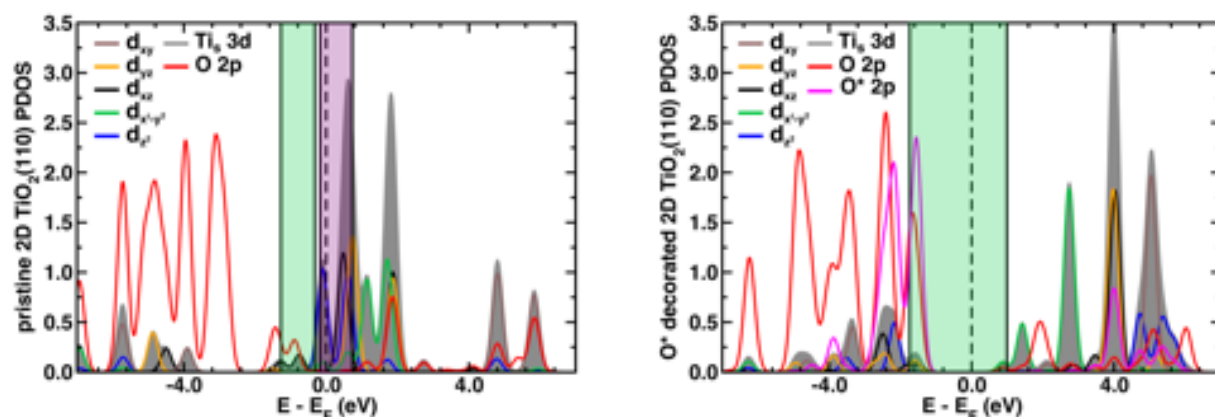


Figure S12. Γ -point projected density of states (PDOS) of all $\text{Ti}_s(3d)$ atomic orbitals (grey shaded region) and of all coordinating $\text{O}(2p)$ atomic orbitals (red solid line) in pristine (left) and O^* -decorated (right) 2D $\text{TiO}_2(110)$. PDOS for the adsorbate $\text{O}^*(2p)$ atomic orbitals is shown in pink and for the $\text{Ti}_s 3d_{xy}$, $3d_{yz}$, $3d_{xz}$, $3d_{x^2-y^2}$ and $3d_{z^2}$ atomic orbitals are shown in brown, orange, black, green and blue respectively. A vertical black dashed line indicates the Fermi level (E_f) for each system. Green transparent region represents the fractionality-based best selected states for constructing the molecular projectors within the Wannier localization scheme, whereas the purple transparent region represents the physically motivated alternate selection of states. Note that alternate states were selected for only the pristine 2D TiO_2 model.

Table S14. Atomic orbital (AO) contributions from the $\text{Ti}_s(3d)$ and $\text{O}(2p)$ orbitals for all plane-wave states (i.e., “molecular orbitals”, labeled by their band index) available for Wannier function construction in pristine 2D TiO_2 (110). All AO contributions are computed at the Γ -point using their projections on the AOs and are listed as a percentage. The columns $\text{Ti}_s(3d)$ and $\text{O}(2p)$ show the sum of contributions from all the individual d and p AOs respectively. $\text{Ti}_s(3d_{xz})$ and $\text{Ti}_s(3d_{yz})$ contributions are listed separately. Contributions from $\text{O}(2s)$ AOs, $\text{Ti}_s(3s/3p/4s)$ AOs or any Ti_b or Ti_u AOs are not shown. Any other missing contribution was not suitably described by the atomic projections available in the pseudopotentials being used. The five contiguous states selected based on fractionality analysis are highlighted in green and the states selected based on physical justification are highlighted in purple.

Band Index	$\text{Ti}_s(3d)$ (%)	$\text{Ti}_s(3d_{xz})$ (%)	$\text{Ti}_s(3d_{yz})$ (%)	$\text{O}(2p)$ (%)	Band Index	$\text{Ti}_s(3d)$ (%)	$\text{Ti}_s(3d_{xz})$ (%)	$\text{Ti}_s(3d_{yz})$ (%)	$\text{O}(2p)$ (%)
1	0	0	0	1.2	39	0	0	0	97.6
2	0	0	0	2	40	1.1	0	1.1	94.4
3	0	0	0	1.6	41	0	0	0	83.2
4	0	0	0	2	42	0.2	0	0	95.2
5	0	0	0	2.4	43	3.9	3.9	0	75.8
6	0	0	0	0.4	44	0	0	0	77.6
7	0	0	0	0	45	0	0	0	98
8	0	0	0	0	46	6.3	6.3	0	85.8
9	0	0	0	1.6	47	0	0	0	98
10	0	0	0	2.4	48	0	0	0	98.4
11	0	0	0	2.4	49	40.7	0	0	0
12	0	0	0	0.8	50	43.2	43.2	0	13.2
13	0	0	0	0.8	51	42.6	0	0	1.6
14	0	0	0	0	52	49.8	0	49.8	0
15	0	0	0	2	53	34.1	0	0	7.6
16	0	0	0	1.2	54	45.3	0	0	6
17	2	0	0	0.4	55	36.2	36.2	0	25.2
18	5.5	0	0	0	56	34	0	34	31.2
19	0	0	0	0	57	4.2	0	0	0.8
20	0	0	0	0	58	0	0	0	5.6
21	0	0	0	1.2	59	0.8	0	0	12.4
22	0	0	0	0	60	0	0	0	2.4
23	0	0	0	0.8	61	0	0	0	28.4
24	0	0	0	0	62	1.3	1.3	0	22.4
25	9.8	0	0	66	63	0	0	0	0.8
26	17.5	0	0	64	64	5	0	0	3.2
27	7	0	0	75.2	65	35.6	0	0	19.6
28	0	0	0	85.6	66	0	0	0	18.4
29	14.3	0	14.3	70.4	67	0.4	0	0	6
30	0	0	0	84.4	68	28	0	0	34.8
31	8.6	8.6	0	76	69	2	0	0	11.2
32	0	0	0	96.4	70	0	0	0	0
33	8.7	0	0	78.8	71	0	0	0	16
34	0	0	0	68	72	0	0	0	5.6
35	0	0	0	73.6	73	2.5	0	0	6.4
36	0	0	0	96.8	74	0	0	0	36.4
37	0	0	0	63.6	75	0	0	0	0.4
38	0	0	0	93.6					

Table S15. Atomic orbital (AO) contributions from the $Ti_s(3d)$, $O(2p)$ and $O^*(2p)$ orbitals for all plane-wave states (i.e., “molecular orbitals”, labeled by their band index) available for Wannier function construction in O^* -decorated 2D TiO_2 (110). All AO contributions are computed at the Γ -point using their projections on the AOs and are given as a percentage. The $Ti_s(3d)$ and $O(2p)$ or $O^*(2p)$ columns give the sum of contributions from all the individual d and p AOs respectively. $Ti_s(3d_{xz})$ and $Ti_s(3d_{yz})$ contributions are listed separately. Contributions from $O(2s)$ AOs, $Ti_s(3s/3p/4s)$ AOs or any Ti_b or Ti_u AOs are not shown. Any other missing contribution was not suitably described by the atomic projections available in the pseudopotentials being used. The five contiguous states selected based on fractionality analysis are highlighted in green.

Band Index	$Ti_s(3d)$ (%)	$Ti_s(3d_{xz})$ (%)	$Ti_s(3d_{yz})$ (%)	$O^*(2p)$ (%)	$O(2p)$ (%)	Band Index	$Ti_s(3d)$ (%)	$Ti_s(3d_{xz})$ (%)	$Ti_s(3d_{yz})$ (%)	$O^*(2p)$ (%)	$O(2p)$ (%)
1	0	0	0	0	1.6	39	2.5	0	0	0.6	82.1
2	0	0	0	0	1.7	40	16.2	0	0	0	78.8
3	0	0	0	0	3	41	0.4	0	0	0.2	77.1
4	0	0	0	1.1	0.8	42	3	0	3	8.7	83.3
5	0	0	0	0	2.9	43	4	4	0	2.8	80
6	0	0	0	0	2	44	11.1	11.1	0	32	50.7
7	0	0	0	0	0	45	6.6	0	6.6	6.7	78.9
8	0	0	0	0	1.2	46	0.8	0	0	0	89.2
9	0	0	0	0	0.8	47	17.9	0	0	69.6	5.2
10	0	0	0	0	1.8	48	2.3	2.3	0	6.4	87.2
11	0	0	0	0	2.4	49	0.2	0.2	0	0.1	96.2
12	0	0	0	0	0.8	50	4.2	0	4.2	52.8	40.2
13	0	0	0	0	2.6	51	2.5	2.5	0	35.5	54.7
14	0	0	0	2.1	0	52	2.9	0	0	0.1	13.1
15	0	0	0	0.2	0.8	53	1	0	0	0	84.1
16	0	0	0	0.2	0.8	54	17.7	0	0	0	4
17	0	0	0	0	7.6	55	0.3	0.3	0	0.5	20.7
18	0.7	0	0	0	0	56	0.6	0	0.6	0	20
19	2.8	0	0	0	0	57	0.3	0	0	0	3.6
20	0	0	0	0	0.8	58	0.8	0	0	0	15.9
21	0.3	0	0.3	0	0	59	2.7	0	0	0	6
22	0	0	0	0	0.4	60	66.5	0	0	0	4
23	0.2	0.2	0	0	0.6	61	2.6	2.6	0	0.7	25.3
24	0	0	0	0	3	62	6	6	0	2.4	21
25	5.4	0	0	0.2	0	63	34.4	0	34.4	7.6	11.4
26	0.1	0	0	0	80.8	64	34.4	0	34.4	8.4	13.2
27	5.3	0	0	0	66.6	65	65.9	65.9	0	15.5	7.3
28	0.1	0.1	0	0	80.7	66	0.8	0	0	0.7	3.9
29	0	0	0	0	82.2	67	21.9	0	0	7.4	9.6
30	0.7	0	0.7	0.2	68.9	68	71.2	0	0	0	20
31	2.9	0	2.9	0.4	74.8	69	3.4	0	0	1	0.8
32	2.7	0	0	0	77.7	70	5.7	0	5.7	1.8	20.5
33	4.1	0	0	0	66.8	71	18.1	0	0	7.7	3.2
34	2.6	2.6	0	2.6	73.3	72	11.3	0	0	3.6	8.4
35	0.8	0.8	0	0.1	91.7	73	1.1	0	0	0.3	20.5
36	5.9	0	5.9	12.1	68.5	74	1.4	0	0	0	31.2
37	0	0	0	0.2	75.9	75	0	0	0	0	31.3
38	3	0	0	1.2	83.7						

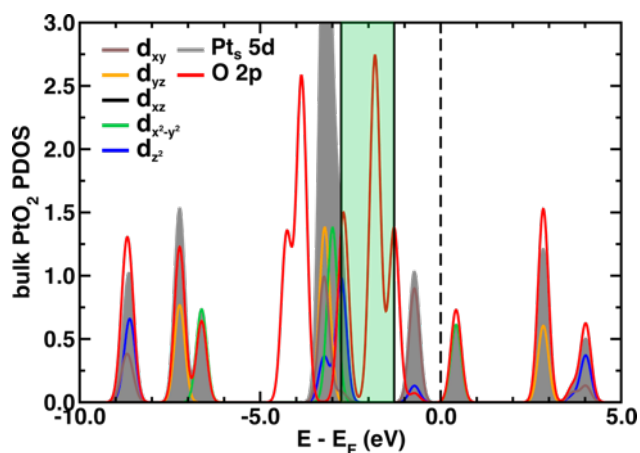


Figure S13. Γ -point projected density of states (PDOS) of all $\text{Pt}_s(5d)$ atomic orbitals (gray shaded region) and of the coordinating $\text{O}(2p)$ atomic orbitals in the (110) plane (red solid line) for bulk rutile PtO_2 . The PDOS for the $\text{Pt}_s 5d_{xy}$, $5d_{yz}$, $5d_{xz}$, $5d_{x^2-y^2}$, and $5d_{z^2}$ atomic orbitals are shown in brown, orange, black, green, and blue, respectively. The vertical black dashed line indicates the Fermi level (E_f). The green transparent region represents the fractionality-based best selected states for constructing the molecular projectors within the Wannier localization scheme for improving surface energy sensitivity.

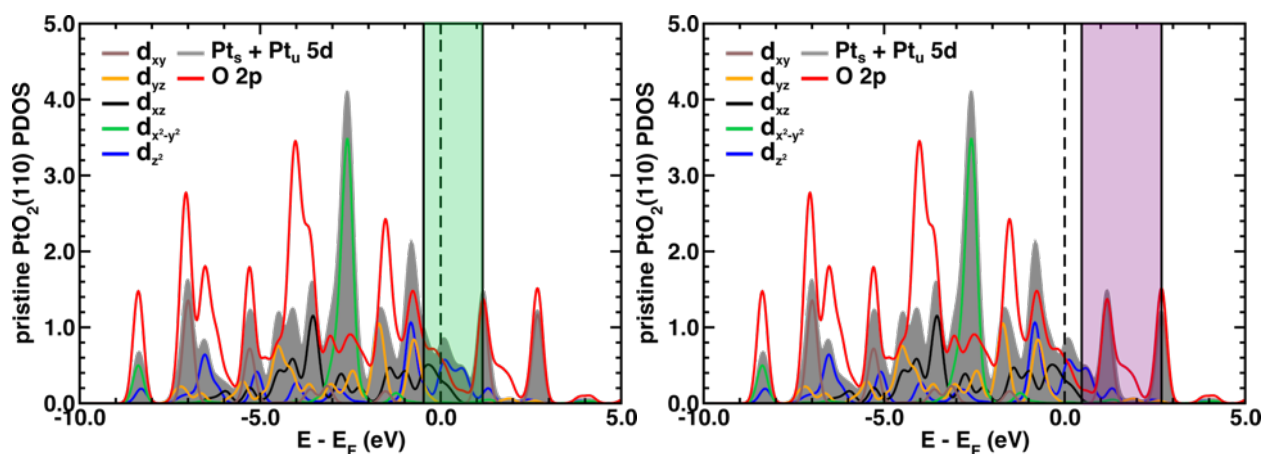


Figure S14. Γ -point projected density of states (PDOS) of all $\text{Pt}_s(5d)$ and $\text{Pt}_u(5d)$ atomic orbitals (grey shaded region) and of the coordinating $\text{O}(2p)$ atomic orbitals in the (110) plane (red solid line) for pristine $\text{PtO}_2(110)$. The PDOS for the $\text{Pt } 5d_{xy}$, $5d_{yz}$, $5d_{xz}$, $5d_{x^2-y^2}$, and $5d_{z^2}$ atomic orbitals are shown in brown, orange, black, green, and blue, respectively. The vertical black dashed line indicates the Fermi level (E_f). The green transparent region (left) and purple transparent region (right) represents the fractionality-based best selected states for constructing the molecular projectors within the Wannier localization scheme for improving surface energy sensitivity and for improving adsorption energy sensitivity, respectively.

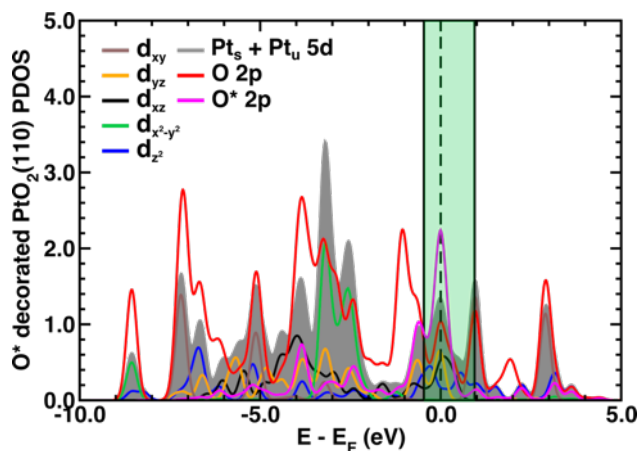


Figure S15. Γ -point projected density of states (PDOS) of all $\text{Pt}_s(5d)$ and $\text{Pt}_u(5d)$ atomic orbitals (grey shaded region) and of all coordinating $\text{O}(2p)$ atomic orbitals in the (110) plane (red solid line) in O^* -decorated $\text{PtO}_2(110)$. The PDOS for the adsorbate $\text{O}^*(2p)$ atomic orbitals are shown in pink and for the $\text{Pt } 5d_{xy}$, $5d_{yz}$, $5d_{xz}$, $5d_{x^2-y^2}$, and $5d_{z^2}$ atomic orbitals are shown in brown, orange, black, green, and blue, respectively. The vertical black dashed line indicates the Fermi level (E_f) for each system. The green transparent region represents the fractionality-based best selected states for constructing the molecular projectors within the Wannier localization scheme for improving adsorption energy sensitivity.

Table S16. Atomic orbital (AO) contributions from the $Pt_s(5d)$, $Pt_u(5d)$, and top surface layer $O(2p)$ orbitals for the fractionality-based best selected plane-wave states (i.e., “molecular orbitals”, labeled by their band index) for Wannier function construction in pristine $PtO_2(110)$ for improving surface energy sensitivity and for improving adsorption energy sensitivity. All AO contributions are computed at the Γ -point using their projections on the AOs and are given as a percentage. The columns $Pt(5d)$ and $O(2p)$ contain the sum of contributions from all the individual d and p AOs respectively. $O(2p_z)$ AO contributions are listed separately. Contributions from $O(2s)$ AOs, $Pt_s(6s/6p)$ AOs, $Pt_u(6s/6p)$ AOs or from the AOs of any other Pt or O atoms in the surface model are not shown. Any missing contribution (i.e., rows that sum up to less than 100%) was not suitably described by the atomic projections available in the pseudopotentials being used. The Fermi level lies between the bands indexed 174 (i.e., the HOMO) and 175 (i.e., the LUMO), both of which are highlighted in bold.

Surface Energy Sensitivity					Adsorption Energy Sensitivity				
Band Index	$Pt_s(5d)$ (%)	$Pt_u(5d)$ (%)	$O(2p)$ (%)	$O(2p_z)$ (%)	Band Index	$Pt_s(5d)$ (%)	$Pt_u(5d)$ (%)	$O(2p)$ (%)	$O(2p_z)$ (%)
168	5.9	5.9	16.8	9.6	182	3	3	8.2	7
169	3.8	3.8	8	8	183	6.7	6.7	4.4	4.4
170	1.3	1.3	13.4	0	184	1.5	1.5	2.2	1.4
171	1.3	1.3	3.8	2.8	185	0	0	0	0
172	4.7	4.7	10.4	10	186	0	0	0	0
173	1.7	1.7	10.8	7.2	187	23.9	23.9	41.2	8.8
174	0	0	9.2	2.8	188	0	0	0	0
175	1.1	1.1	1.4	0	189	0.5	0.5	12	8
176	8.9	8.9	6.8	6.8	190	1.5	1.5	8	7.2
177	0.5	0.5	21.4	0	191	1.7	1.7	7.6	6.8
178	1.9	1.9	12.2	6	192	1.1	1.1	13.6	6.8
179	0.5	0.5	15.4	0	193	0	0	8.2	0.8
180	3.2	3.2	6	5.2	194	0.3	0.3	14.8	2
181	1.2	1.2	6	2.8	195	0.7	0.7	10.2	1.6
182	3	3	8.2	7	196	0.4	0.4	3.6	0.4
183	6.7	6.7	4.4	4.4	197	0.9	0.9	2	0
184	1.5	1.5	2.2	1.4	198	0.6	0.6	0	0
185	0	0	0	0	199	0	0	1.4	0
186	0	0	0	0	200	0.3	0.3	3	3
187	23.9	23.9	41.2	8.8	201	21.1	21	54	0

Table S17. Atomic orbital (AO) contributions from the $\text{Pt}_s(5d)$, $\text{Pt}_u(5d)$, $\text{O}^*(2p)$ and top surface layer $\text{O}(2p)$ orbitals for the fractionality-based best selected plane-wave states (i.e., “molecular orbitals”, labeled by their band index) for Wannier function construction in O^* -decorated $\text{PtO}_2(110)$ for improving adsorption energy sensitivity. All AO contributions are computed at the Γ -point using their projections on the AOs and are given as a percentage. The columns $\text{Pt}(5d)$ and $\text{O}(2p)$ contain the sum of contributions from all the individual d and p AOs respectively. Contributions from $\text{O}(2s)$ AOs, $\text{Pt}_s(6s/6p)$ AOs, $\text{Pt}_u(6s/6p)$ AOs or from the AOs of any other Pt or O atoms in the surface model are not shown. Any other missing contribution (i.e., rows that sum up to less than 100%) was not suitably described by the atomic projections available in the pseudopotentials being used. The Fermi level lies between the bands indexed 177 (i.e., the HOMO) and 178 (i.e., the LUMO), both of which are highlighted in bold.

Band Index	$\text{Pt}_s(5d)$ (%)	$\text{Pt}_u(5d)$ (%)	$\text{O}(2p)$ (%)	$\text{O}^*(2p)$ (%)
170	0.3	3.9	7.8	13.8
171	0.4	2.5	15.7	1
172	0.2	14.3	3.7	1.1
173	0.7	1.8	2.9	6.9
174	1.6	0	0	7.4
175	2.4	1.5	9	2
176	3.2	0.5	9.6	12.8
177	18	4.9	15.8	44.8
178	3.8	1	13.6	2.2
179	1.3	1.9	8.5	3.3
180	1.9	2.8	2.7	3.7
181	3.8	0.3	9.9	15.8
182	0.2	0.6	18.4	0.6
183	3.1	4.1	19.1	4.4
184	2.3	3	9.6	2.1
185	0	2	10.9	0.4
186	0.8	10.3	4.5	0.2
187	1.6	0.9	4.4	1.6
188	0.3	0.2	0	0
189	0	0	0	0

Table S18. Atomic orbital (AO) contributions from the $Ti_s(3d)$, $Ti_u(3d)$, and top surface layer $O(2p)$ orbitals for the fractionality-based best selected plane-wave states (i.e., “molecular orbitals”, labeled by their band index) for Wannier function construction in pristine $TiO_2(110)$ for improving surface energy sensitivity and for improving adsorption energy sensitivity. All AO contributions are computed at the Γ -point using their projections on the AOs and are given as a percentage. The $Ti(3d)$ and $O(2p)$ columns contain the sum of contributions from all the individual d and p AOs respectively. $O(2p_z)$ AO contributions are listed separately. Contributions from $O(2s)$ AOs, $Ti_s(3s/3p/4s)$ AOs, $Ti_u(3s/3p/4s)$ AOs or from the AOs of any other Ti or O atoms in the surface model are not shown. Any missing contribution (i.e., rows that sum up to less than 100%) was not suitably described by the atomic projections available in the pseudopotentials being used. The Fermi level lies between the bands indexed 192 (i.e., the HOMO) and 193 (i.e., the LUMO), both of which are highlighted in bold.

Surface Energy Sensitivity					Adsorption Energy Sensitivity				
Band Index	$Ti_s(3d)$ (%)	$Ti_u(3d)$ (%)	$O(2p)$ (%)	$O(2p_z)$ (%)	Band Index	$Ti_s(3d)$ (%)	$Ti_u(3d)$ (%)	$O(2p)$ (%)	$O(2p_z)$ (%)
181	0	0	0	0	192	0.1	0.1	4	1.2
182	0.2	0.2	3	0	193	1.3	1.3	0.8	0.8
183	0	0	27	0	194	0.8	0.8	0.4	0.4
184	0.3	0.3	6.2	6.2	195	9.7	9.7	1.8	0
185	0	0	7.6	2.4	196	13.4	13.4	1.6	0
186	0	0	10	0	197	17.1	17.1	2	0
187	0.1	0.1	15.4	0	198	7.7	7.7	1.2	0
188	0.2	0.2	7.2	0	199	1.3	1.3	0	0
189	0.7	0.7	14.4	10.4	200	0	0	0	0
190	0.2	0.2	47.4	8.8	201	0	0	0	0
191	0	0	35.8	2.4	202	15.2	15.2	2.4	0
192	0.1	0.1	4	1.2	203	0	0	0	0
193	1.3	1.3	0.8	0.8	204	4.7	4.7	1.8	1.2
194	0.8	0.8	0.4	0.4	205	0	0	0	0
195	9.7	9.7	1.8	0	206	0.9	0.9	1.6	0
196	13.4	13.4	1.6	0	207	18.7	18.7	2.8	0
197	17.1	17.1	2	0	208	17.7	17.7	2.8	0
198	7.7	7.7	1.2	0	209	0	0	0	0
199	1.3	1.3	0	0	210	10.5	10.5	3.6	2.8
200	0	0	0	0	211	0	0	0	0

Table S19. Atomic orbital (AO) contributions from the $Ti_s(3d)$, $Ti_u(3d)$, $O^*(2p)$ and top surface layer $O(2p)$ orbitals for the fractionality-based best selected plane-wave states (i.e., “molecular orbitals”, labeled by their band index) for Wannier function construction in O^* decorated $TiO_2(110)$ for improving adsorption energy sensitivity. All AO contributions are computed at the Γ -point using their projections on the AOs and are given as a percentage. The $Ti(3d)$ and $O(2p)$ columns contain the sum of contributions from all the individual d and p AOs respectively. Contributions from $O(2s)$ AOs, $Ti_s(3s/3p/4s)$ AOs, $Ti_u(3s/3p/4s)$ AOs or from the AOs of any other Ti or O atoms in the surface model are not shown. Any other missing contribution (i.e., rows that sum up to less than 100%) was not suitably described by the atomic projections available in the pseudopotentials being used. The Fermi level lies between the bands indexed 194 (i.e., the HOMO) and 195 (i.e., the LUMO), both of which are highlighted in bold.

Band Index	$Ti_s(3d)$ (%)	$Ti_u(3d)$ (%)	$O(2p)$ (%)	$O^*(2p)$ (%)
189	0.9	0.5	29.1	1.2
190	0.1	0.3	0	1.3
191	0	0	0	0
192	0	0	0	0
193	4.7	2.3	28.4	51.9
194	0	0	0.7	0.2
195	0	0.1	47.2	7.5
196	0.2	0.7	33.4	7.8
197	0	0	0	0
198	0	0	0	0
199	0	0	0	0
200	0	0	0	0
201	0	0	0	0
202	0	0	0	0
203	0	0	0	0
204	0	0.8	0	0
205	0	0	0	0
206	0.4	4.2	0	0.5
207	0.1	3.8	0.1	0
208	0	0	0	0

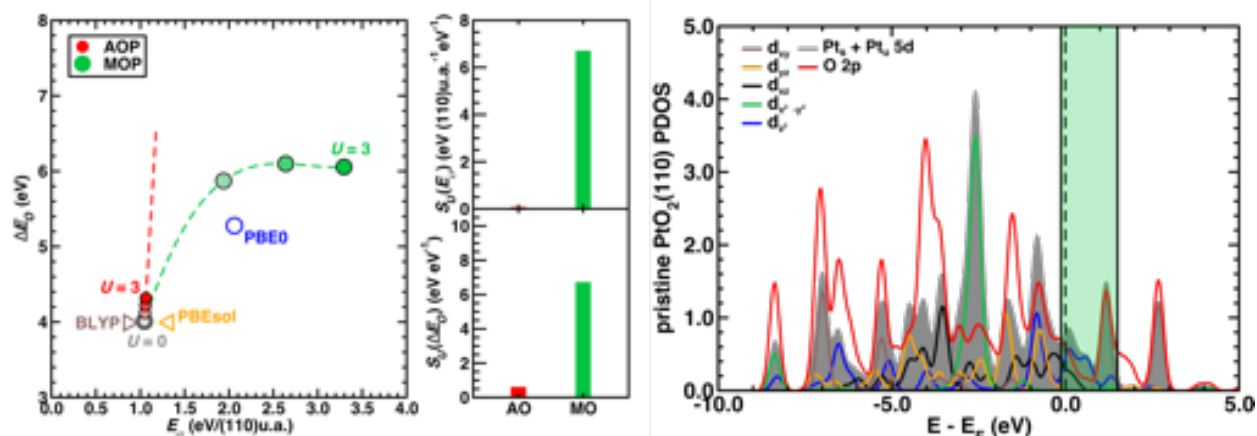


Figure S16. (left) ΔE_O (in eV) versus E_σ (in eV/(110)u.a.) for PtO₂ (110) computed using Pt 5d AOPs (shaded red circles) and MOPs (shaded green circles) at integer values of U from 0 to 3 eV with a dashed line indicating a fit between these points. Values from BLYP^{8,9} (brown triangle), PBEsol¹⁰ (orange triangle), and PBE0^{4,6} (blue circle) were obtained from Ref. 1 using a localized basis set and shifted to align our PBE plane-wave basis set value and the PBE localized basis set value from Ref. 1. Fractionality-selected best MOPs were used for the bulk and O* decorated PtO₂ models and MOPs were chosen for the pristine PtO₂ slab to be identical in both surface formation and adsorption calculations. (middle) Linearized sensitivities of E_σ (top, in eV/(110) unit area per eV of U) and of ΔE_O (bottom, in eV per eV of U) computed with AOPs (red bars) and MOPs (green bars). (right) Γ -point projected density of states (PDOS) of all Pt_s(5d) and Pt_t(5d) atomic orbitals (grey shaded region) and of the coordinating O(2p) atomic orbitals in the (110) plane (red solid line) for pristine PtO₂(110). The PDOS for the Pt 5d_{xy}, 5d_{yz}, 5d_{xz}, 5d_{x²-y²}, and 5d_{z²} atomic orbitals are shown in brown, orange, black, green, and blue, respectively. The vertical black dashed line indicates the Fermi level (E_F). The green transparent region represents the chosen alternate states used for constructing the molecular projectors within the Wannier localization scheme for improving both surface energy and adsorption energy sensitivities by maximizing the geometric mean in $\Delta \text{Tr}[\mathbf{n}(1-\mathbf{n})]$ for both quantities.

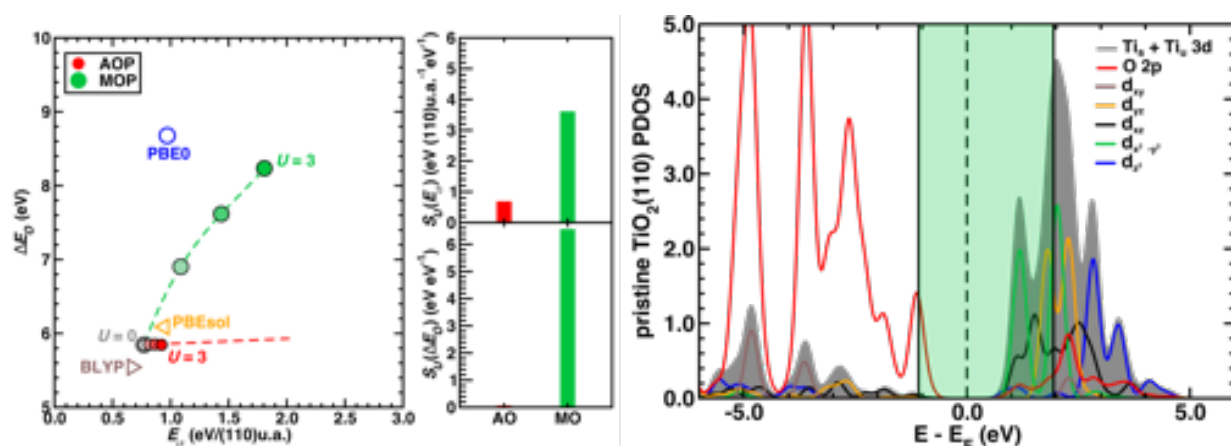


Figure S17. (left) ΔE_O (in eV) versus E_σ (in eV/(110)u.a.) for TiO_2 (110) computed using Ti $3d$ AOPs (shaded red circles) and MOPs (shaded green circles) at integer values of U from 0 to 3 eV with a dashed line indicating the trend between these points. Values from BLYP^{8,9} (brown triangle), PBEsol¹⁰ (orange triangle), and PBE0^{4,6} (blue circle) were obtained from Ref. 1 using a localized basis set and shifted to align our PBE plane-wave basis set value and the PBE localized basis set value from Ref. 1. Fractionality-selected best MOPs were used for the bulk and O* decorated TiO_2 models and MOPs were chosen for the pristine TiO_2 slab to be identical in both surface formation and adsorption calculations. (middle) Linearized sensitivities of E_σ (top, in eV/(110) unit area per eV of U) and of ΔE_O (bottom, in eV per eV of U) computed with AOPs (red bars) and MOPs (green bars). (right) Γ -point projected density of states (PDOS) of all $\text{Ti}_s(3d)$ and $\text{Ti}_t(3d)$ atomic orbitals (grey shaded region) and of the coordinating O($2p$) atomic orbitals in the (110) plane (red solid line) for pristine $\text{TiO}_2(110)$. The PDOS for the Ti $3d_{xy}$, $3d_{yz}$, $3d_{xz}$, $3d_{x^2-y^2}$ and $3d_{z^2}$ atomic orbitals are indicated in brown, orange, black, green, and blue, respectively. The vertical black dashed line denotes the Fermi level (E_f). The green transparent region represents the chosen alternate states used for constructing the molecular projectors within the Wannier localization scheme for improving both surface energy and adsorption energy sensitivities by maximizing the geometric mean in $\Delta\text{Tr}[\mathbf{n}(1-\mathbf{n})]$ for both quantities.

References

- (1) Zhao, Q.; Kulik, H. J. Stable Surfaces That Bind Too Tightly: Can Range Separated Hybrids or Dft+U Improve Paradoxical Descriptions of Surface Chemistry? *J. Phys. Chem. Lett.* **2019**, *10*, 5090.
- (2) <http://www.quantum-espresso.org/pseudopotentials>. (Accessed June 13, 2021).
- (3) Giannozzi, P.; Andreussi, O.; Brumme, T.; Bunau, O.; Nardelli, M. B.; Calandra, M.; Car, R.; Cavazzoni, C.; Ceresoli, D.; Cococcioni, M. et al. Advanced Capabilities for Materials Modelling with Quantum Espresso. *J. Phys.: Condens. Matter* **2017**, *29*, 465901.
- (4) Perdew, J. P.; Ernzerhof, M.; Burke, K. Rationale for Mixing Exact Exchange with Density Functional Approximations. *J. Chem. Phys.* **1996**, *105*, 9982.
- (5) Ernzerhof, M.; Scuseria, G. E. Assessment of the Perdew-Burke-Ernzerhof Exchange-Correlation Functional. *J. Chem. Phys.* **1999**, *110*, 5029.

- (6) Adamo, C.; Barone, V. Toward Reliable Density Functional Methods without Adjustable Parameters: The Pbe0 Model. *J. Chem. Phys.* **1999**, *110*, 6158.
- (7) Batsanov, S. S. Van Der Waals Radii of Elements. *Inorg. Mater.* **2001**, *37*, 871.
- (8) Becke, A. D. Density-Functional Exchange-Energy Approximation with Correct Asymptotic-Behavior. *Phys. Rev. A* **1988**, *38*, 3098.
- (9) Lee, C. T.; Yang, W. T.; Parr, R. G. Development of the Colle-Salvetti Correlation-Energy Formula into a Functional of the Electron-Density. *Phys. Rev. B* **1988**, *37*, 785.
- (10) Perdew, J. P.; Ruzsinszky, A.; Csonka, G. I.; Vydrov, O. A.; Scuseria, G. E.; Constantin, L. A.; Zhou, X. L.; Burke, K. Restoring the Density-Gradient Expansion for Exchange in Solids and Surfaces (Vol 100, Art No 136406, 2008). *Phys. Rev. Lett.* **2009**, *102*, 039902.